

Cover Page



Universiteit Leiden



The handle <http://hdl.handle.net/1887/81787> holds various files of this Leiden University dissertation.

Author: Sunku, K.

Title: Connecting dots between natural and artificial photosynthesis : magnetic resonance studies on light harvesting and the water oxidation reaction centre

Issue Date: 2019-12-13

Connecting Dots between Natural and Artificial Photosynthesis

Kiran Sunku

Connecting Dots between Natural and Artificial Photosynthesis

Magnetic Resonance Studies on Light Harvesting and the Water Oxidation
Reaction Centre

Proefschrift

ter verkrijging van
de graad van Doctor aan de Universiteit Leiden,
op gezag van Rector Magnificus prof.mr. C.J.J.M. Stolker,
volgens besluit van het College voor Promoties
te verdedigen op 13 december 2019
klokke 13.45 uur

door

Kiran Sunku

geboren te Dharmavaram, India

in 1986

Promotor: Prof. dr. H.J.M. de Groot

Copromotor: Dr. Anjali Pandit

Promotiecommissie: Prof.dr. H.S. Overkleeft (voorzitter)

Prof.dr. M. Ubbink (secretaris)

Overige commissieleden: Prof.dr. Joanna Kargul

Prof.dr. Alfred Holzwarth

This research was financed in part by the Dutch Ministry of Economic affairs as part of the Biosolar Cells research project number C1.6.



**Universiteit
Leiden**
The Netherlands

ISBN: 978-94-92597-36-6

Dedicated to Simon de Vries

Table of Contents

Chapter 1	General Introduction	9
1.1.	Photosynthesis	10
1.2.	Photosystem II and Water Oxidation Complex	10
1.3.	Light Harvesting Complex II	11
1.4.	Rapid Freeze Quenching	12
1.5.	Solid State NMR	13
1.5.1.	Cross-Polarization	14
1.5.2.	Heteronuclear Correlation Experiment	15
1.6.	Electron Paramagnetic Resonance	16
1.7.	References	17
Chapter 2	Design of a Novel Device Enabling Freeze-quench Trapping of Laser Flash Activated Photosystem II	23
2.1.	Intermediates	24
2.2.	Introduction	26
2.2.1.	Materials and Methods	26
2.2.2.	Preparation of Photosystem II Membrane Particles	27
2.2.3.	EPR Experiments	27
2.3.	Rapid Freeze Quenching	28
2.3.1.	Results and Discussion	28
2.3.2.	The Construction of Flash-RFQ Setup EPR Responses of Flash Excited Freeze Quenched	30
2.4.	Photosystem II	34
2.5.	Conclusion	35
2.6.	References	40
	Appendix	
Chapter 3	Insights in The Photoprotective Switch of The Major Light- Harvesting Complex II (LHCII): A Preserved Core of Arginine-glutamate Interlocked Helices Complemented by Adjustable Loops	41
3.1.	Introduction	43
3.2.	Materials and Methods	45

3.2.1.	Isotope Enrichment and Purification of LHCII Trimers	45
3.2.2.	Fluorescence Experiments	46
3.2.3.	Solid-state NMR Experiments	46
3.2.4.	Density Functional Theory Calculations	47
3.3.	Results	47
3.3.1.	Fluorescence Conditions of LHCII in The Detergent-solubilized and Aggregated State	47
3.3.2.	Arg NMR Responses for LHCII in Its Active and Dissipative State	48
3.4.	Discussion	51
3.4.1.	Upfield Shifted NMR Responses are Explained by Chl Ringcurrent Shifts for R70 and R185	52
3.4.2.	In Quenched LHCII, R25 Changes Its Backbone Conformation	55
3.4.3.	Stability of The Interlocked A and B Helices in The LHCII Core: Implications for Possible Conformational Changes	56
3.5.	Conclusion	58
3.6.	References	60
Chapter 4	Structure Determination of Self-aggregated and Semi Synthetically Prepared Zn ³¹-amino Chlorin with MAS NMR and Molecular Modelling	67
4.1.	Introduction	68
4.2.	Materials and Methods	69
4.2.1.	Preparation of ZnChl Aggregates	69
4.2.2.	Solid State NMR Experiments	70
4.2.3.	Molecular Modelling	70
4.3.	Results and Discussion	70
4.3.1.	Absorption Spectra of Monomer and Aggregates of ZnChl	70
4.3.2.	NMR Responses for Monomer and Aggregates of ZnChl	71
4.4.	Conclusion	79
4.5.	References	80
4.6.	Appendix	84
Chapter 5	Conclusions and Outlook	87

Appendices	91
Summary	93
Samenvatting	95
Curriculum Vitae	97
Acknowledgements	98
Publication list	100

Abbreviations

NADP – Nicotinamide adenine dinucleotide phosphate
ATP – Adenosine triphosphate
PS II – Photosystem II
OEC – Oxygen Evolving Complex
LHC II – Light Harvesting Complex II
NPQ – Nonphotochemical quenching
EPR – Electron Paramagnetic Resonance
HPLC – High-performance liquid chromatography
RFQ – Rapid freeze quenching
NMR – Nuclear Magnetic Resonance
CP-MAS – Cross Polarization - Magic angle spinning
FSLG – Frequency switched Lee-Goldburg
HETCOR – Heteronuclear Correlation
XAFS – X-ray absorption fine structure
HEPES – 4-(2-hydroxyethyl)-1-piperazineethanesulfonic acid
EDTA – Ethylenediaminetetraacetic acid
MES – 2-(N-morpholino)ethanesulfonic acid
DMSO – Dimethyl sulfoxide
PPBQ – Phenyl-p-benzoquinone
PEEK – Polyetheretherketone
MHQ – Microsecond freeze-hyperquenching
 β -DM – Decyl β -D-maltopyranoside

General Introduction

Chapter 1

1.1. Photosynthesis

After 3 billion years of evolution, nature has provided us with a wonderful machinery to convert sunlight into storable chemical energy: photosynthesis^{1,2}. In the process of photosynthesis the waste product is oxygen, which sustains the life of oxygen-consuming organisms. Photosynthesis takes place in many different organisms. In higher plants and green algae, photosynthesis occurs in thylakoid membranes, which are present in chloroplasts. The stacked membranes are called grana whereas non-stacked membranes are known as stromal thylakoids³.

Photosynthesis involves three consecutive steps. In the first step light energy is absorbed by light harvesting antenna complexes and funneled to a reaction center^{4,5}. In the second step, the absorbed light energy is converted and stored into chemical forms as NADPH and ATP^{6,7}. The third step involves using NADPH and ATP to assimilate the carbon or carbon fixation. In this final step the energy is stored in sugars, which are a form of cellular biochemical energy⁸.

In higher plants, the Photosystem II (PSII) is selectively located in grana thylakoid membranes. It is practically possible to separate and isolate thylakoid membranes that contain mostly PSII by using a detergent-based method^{9,10}. The PSII particles are capable of producing oxygen on illumination in the presence of an external artificial electron acceptor. Such PSII particles are used in our experiments in chapter 2.

1.2. Photosystem II and Water Oxidation Complex

Photosystem II performs water splitting, oxygen release and protonation of plastoquinone to store the electrons extracted from water in a chemical redox carrier. The detailed structure of Photosystem II has been studied and resolved by X-ray crystallography and it has been estimated that the core of the Photosystem II complex contains about 35 Chl molecules, 2 Pheophytins, 11 β -carotenes and more than 20 lipids¹¹⁻¹³. It has been estimated that each Photosystem II converts the energy collected by approximately 200-300 Chl molecules¹⁴⁻¹⁷.

The luminal side of Photosystem II contains the water splitting machine, the oxygen evolving complex. The structure of the OEC has recently been resolved to a resolution of 1.9 Å by X-ray crystallography by Umena *et al.*,¹³. The catalytic site of the OEC contains 4 Mn and a Ca²⁺ ion and Cl⁻ ions, which are required for stabilization of the structure and for proper functioning of the OEC¹⁸⁻²¹.

1.3. Light Harvesting Complex II

All oxygen evolving photosynthesizes, like higher plants and green algae, contain similar organization of their photosynthetic apparatus which appears to be highly conserved across species and taxonomic boundaries during evolution. This functional unit should represent an effective and robust machinery that adheres to a restricted set of key engineering principles to adopt to different growing conditions on Earth and to environmental stresses²²⁻²⁴. Above all, the photosynthetic apparatus must have flexibility with respect to continuously changing radiation conditions during the daily solar cycle and yearly seasonal cycle. Last but not least, short term variations due to different shading conditions must be balanced, for example in light spots on the ground. Understanding the underlying mechanism and high flexibility of light adaptation by the peripheral antenna is a major challenge in photosynthesis research.

The LHC II complex is trimeric and each monomer contains 8 chlorophyll *a*, 6 chlorophyll *b*, 2 luteins, 1 neoxanthin and 1 violaxanthin and the structure of LCH II of pea is shown in Fig.1. LHC II complexes are involved in regulatory mechanisms to avoid photodamage from incoming light energy^{5,25-28}. Under high sunlight conditions, the LHC II antenna can rapidly change from the light harvesting state to a photoprotective state. The excess energy is dissipated as heat, by mechanism called non-photochemical quenching (NPQ)²⁹⁻³². From the LHC II major light harvesting complexes the excitation energy is transferred via the core light-harvesting complexes to the reaction center, where water is oxidized by the Mn cluster of the oxygen evolving complex.

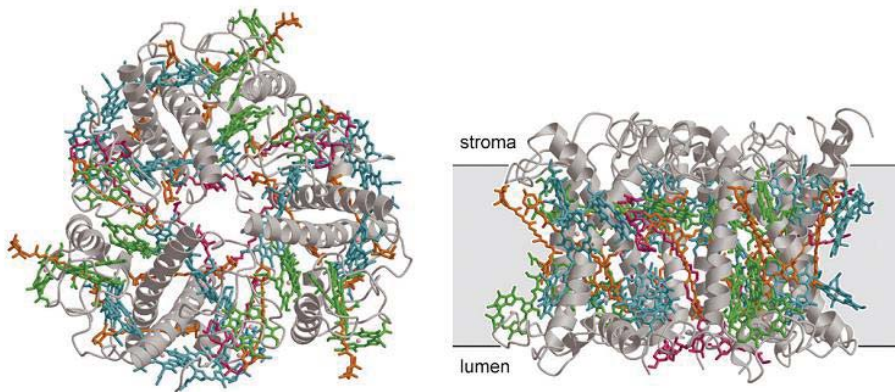


Figure 1. Structure of LHCII of pea²⁷. Top view (left panel) and side view through the membrane (right panel)

1.4. Rapid Freeze Quenching

Rapid Freeze Quenching is one of the few methods that are used to study the catalytic mechanisms of enzymes through the analysis of transient intermediates^{33–37}. Rapid freeze-quenching was developed by Graham, Ballou and Palmer in the nineteen sixties and seventies^{38,39}. Initially the method was developed for studying the redox-enzyme kinetics with EPR spectroscopy, since the continuous and stopped flow methods were not suitable for EPR spectroscopy.

The rapid freeze-quenching set-up is basically a continuous flow instrument. The flow is generated by a drive ram present in HPLC pumps, pushing two syringes, one loaded with enzyme and the other one contains the substrate activate the enzyme reaction. After mixing the sample is delivered through a nozzle to a cryo-bath, where the reaction is rapidly quenched. The sample aging time is varied by changing the length of the nozzle tubing. To quench the reaction either cold isopentane or liquid ethane or liquid nitrogen were used.

The dead-time or minimum total sample aging time τ_a can be formulated as follows,

$$\tau_a = \tau_m + \tau_t + \tau_q$$

In which τ_a is the total aging time of the sample, τ_m is the mixing time, τ_t is the transport time and τ_q is the quenching or freezing time. Rapid freeze-quenching methods generally

Chapter 1

involved 40 μs mixing time, 1 to 2 ms sample delivery time and 4 to 6 ms for the quenching time, yielding a total dead time of 5 to 7 ms⁴⁰⁻⁴³.

By improving the methods used in rapid freeze-quenching the total dead-time was significantly improved to 130 μs by Cherepanov and de Vries⁴⁴. This was achieved by using a stainless steel mixer base with micro-channels of 50 μm . The mixing time was determined at less than 2 μs and the cold isopentane is used as quenching medium.

The RFQ method developed by Cherepanov and Simon de Vries is used in this thesis to study the enzyme mechanisms. The two channels in the mixer were altered to one channel and the Photosystem II sample was illuminated with a high power red laser on the flow path just before quenching. The Photosystem II is quenched most effectively with cold isopentane or liquid nitrogen.

1.5. Solid State NMR

NMR chemical shifts depend on not only the different type of nucleus but also the orientation of nucleus to the static magnetic field B_0 . In liquid state, the molecules exhibit Brownian motion and tumble rapidly in the order of nanoseconds to picoseconds. So the orientation-dependent chemical shift contributions such as chemical shift anisotropy and dipolar interactions are not present. In the solid state, the molecules are rigid and dipolar interactions are present, resulting in a powder like pattern. The NMR signal consists of contributions from molecules in different orientations. This is an important difference between two commonly-used NMR spectroscopies; liquid and solid state NMR.

The powder pattern spectra of Solid State NMR contains a wealth of information, but it lacks site specific information, which are used for characterization of molecules and structure determination of biological samples. To obtain high resolution Solid State NMR spectra we need to remove the anisotropic interactions. This can be achieved by mechanical rotation at high speed at an angle of 54.74° also known as magic angle spinning as shown in fig. 2. The high speed rotation of the sample, which is packed in a rotor oriented at magic angle with respect to the static magnetic field B_0 , results in disappearance of the anisotropic part and removes the anisotropic line broadening resulting in narrow lines^{45,46}.

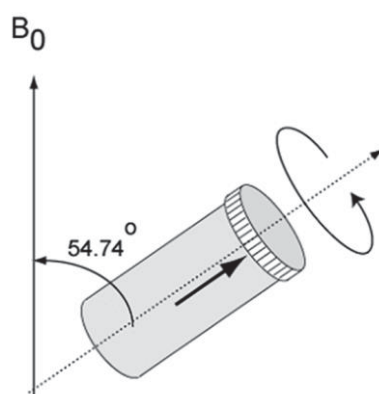


Figure 2. Depiction of the MAS technique. The sample is filled in the rotor and rotated at an angle of 54.74° (magic angle) with respect to magnetic field B_0 .

1.5.1. Cross-Polarization

Cross-polarization method is another important methodology in solid state NMR. There are two types of NMR active nuclei; one type are abundant spin nuclei like ^1H , ^{19}F and the other type are dilute spin nuclei like ^{13}C and ^{15}N . The former nuclei are highly natural abundant and the later ones have low natural abundance. When dealing with dilute spin nuclei in Solid State NMR, generally the signal is weak, due to long spin-relaxation time T_1 . So, large number of scans and averaging of the signals is required in direct polarization experiments for adequate resolution and good signal to noise ratio.

To resolve the problem for dilute spin nuclei in Solid State NMR, cross-polarization methods are used. Cross polarization works by transferring the magnetization from abundant spin nuclei to dilute spin nuclei via their heteronuclear coupling interactions. Cross polarization enhances the magnetization of dilute spin nuclei and increases the signal to noise ratio. So less number of scans is required to get a good signal. Additionally the recycle delay, the time between the scans is reduced. The recycle delay depends on the system to return to equilibrium with B_0 , which is governed by the abundant spin nucleus spin-lattice relaxation time^{47,48}.

Now consider the ^1H - ^{13}C spin pair as an example and they are in a double rotating frame, which means that the magnetization of ^{13}C and ^1H precess about B_0 . The cross polarization process starts with preparation of transverse magnetization of ^1H and it is maintained along the rotating frame x or y axis by using the contact pulse in a given period of time. Simultaneously another contact pulse is given to ^{13}C in order to create

transverse magnetization along its x or y rotating frame axis. The condition for transferring magnetization from ^1H to ^{13}C , the rotating frame energy level separation for the given two nuclei must be same. This is known as Hartmann-Hann matching condition⁴⁹:

$$(\gamma_{1\text{H}})B_1^{1\text{H}} = (\gamma_{13\text{C}})B_1^{13\text{C}}$$

1.5.2. Heteronuclear Correlation experiment

Solid-state cross polarization magic-angle-spinning (CP-MAS) Frequency Switched Lee Goldberg (FSLG) Heteronuclear Correlation (HETCOR) spectra were obtained in a magnetic field of 750 MHz with the pulse sequence as shown below(see Fig.3). This experiment correlates the high-resolution proton spin signals with carbon spin signals. The correlation is obtained when ^1H and ^{13}C nuclei are dipolar coupled, it is therefore a through space correlation. The pulse sequence starts with preparation of a 90° pulse. Subsequently frequency switched Lee-Goldburg (LG) pulses were used to remove the large homonuclear dipolar couplings^{50,51}. Mixing was achieved by the cross polarization pulse during contact time. During this period the magnetization transfers from proton to carbon. During the carbon acquisition the protons are decoupled from carbon by using TPPM decoupling scheme.

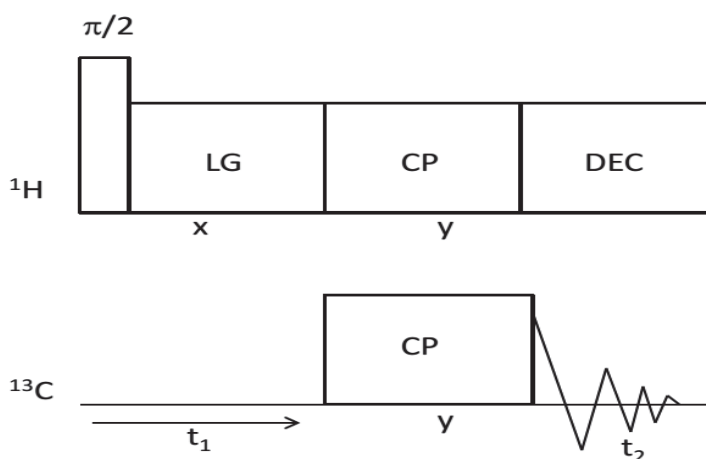


Figure 3. HETCOR ^1H - ^{13}C LG-CP pulse sequence; this pulse sequence starts with 90° preparation pulse followed by the *Lee-Goldburg* decoupling during t_1 . After that cross-polarization pulses are applied in mixing time on both ^1H and ^{13}C . During t_2 ^{13}C FID is observed.

1.6. Electron Paramagnetic Resonance

Electron paramagnetic resonance is called as electron spin resonance. It is a spectroscopic method based on observation of resonance absorption of microwave power by unpaired electron spins in an external magnetic field. When an external magnetic field B applied, a lower energy level is formed in which the electrons are aligned with external magnetic field, and a higher energy level is formed in which the electrons are aligned in the opposite direction of the magnetic field. The energy level difference is given by

$$\Delta E = g\beta B = h\nu$$

By varying the external magnetic field B , the difference in energy levels also changes. Resonance condition emerges when the energy of the microwaves is equal to the difference in energy levels. By observing the EPR spectra, three important parameters can be obtained: the g -factor, the width of the absorbed line and nuclear-hyperfine interactions that give rise to extra lines.

This thesis focus on three projects related to natural and artificial photosynthesis. Major light harvesting complex antenna photo protection mechanism, construction and working of novel flash excitation and rapid freeze quench instrument and structural determination of artificial light antenna complexes by using MAS NMR are the scope of this thesis.

Chapter 2 of this thesis describes the construction of an instrument which combined flash excitation and rapid freeze quenching to study the structural changes during water oxidation mechanism of Photosystem II . The construction involves novel methods in connecting the dark and light parts of flash methodology are explored.

In chapter 3 the role of Arg-Glu ion pair is investigated in conformational switch from light harvesting to photo protection mode in high light conditions of major Light Harvesting Complex II with MAS NMR and selective labeling of Arg.

MAS NMR studies alone can give the self-assembled structure of Zinc amino chlorines was investigated in the chapter 4. Finally chapter 5 discuss about the outlook and future experiments.

1.7. References

1. Barber, J. & Tran, P. D. From natural to artificial photosynthesis. *J. R. Soc. Interface* **10**, 20120984 (2013).
2. Barber, J. Photosystem II: the engine of life. *Q. Rev. Biophys.* **36**, 71–89 (2003).
3. Nugent, J. H. A. Oxygenic Photosynthesis. *Eur. J. Biochem.* **237**, 519–531 (1996).
4. Kühlbrandt, W. Structure and function of the plant light-harvesting complex, LHC-II. *Curr. Opin. Struct. Biol.* **4**, 519–528 (1994).
5. Barros, T. & Kühlbrandt, W. Crystallisation, structure and function of plant light-harvesting Complex II. *Biochim. Biophys. Acta* **1787**, 753–72 (2009).
6. Gao, J., Wang, H., Yuan, Q. & Feng, Y. Structure and Function of the Photosystem Supercomplexes . *Frontiers in Plant Science* **9**, 357 (2018).
7. Vinyard, D. J., Ananyev, G. M. & Charles Dismukes, G. Photosystem II: The Reaction Center of Oxygenic Photosynthesis. *Annu. Rev. Biochem.* **82**, 577–606 (2013).
8. Bender, D. A. Tricarboxylic Acid Cycle. in *Encyclopedia of Food Sciences and Nutrition* (ed. Caballero, B. B. T.-E. of F. S. and N. (Second E.) 5851–5856 (Elsevier, 2003). doi:10.1016/B0-12-227055-X/01363-8
9. Berthold, D. A., Babcock, G. T. & Yocum, C. F. A highly resolved, oxygen-evolving photosystem II preparation from spinach thylakoid membranes. *FEBS Lett.* **134**, 231–234 (1981).
10. Ghanotakis, D. F. & Yocum, C. F. Photosystem II and the Oxygen-Evolving Complex. *Annu. Rev. Plant Physiol. Plant Mol. Biol.* **41**, 255–276 (1990).
11. Guskov, A. *et al.* Cyanobacterial photosystem II at 2.9-Å resolution and the role of quinones, lipids, channels and chloride. *Nat. Struct. & Mol. Biol.* **16**, 334 (2009).
12. Ferreira, K. N., Iverson, T. M., Maghlaoui, K., Barber, J. & Iwata, S. Architecture of the Photosynthetic Oxygen-Evolving Center. *Sci.* **303**, 1831–1838 (2004).
13. Umena, Y., Kawakami, K., Shen, J.-R. & Kamiya, N. Crystal structure of oxygen-evolving photosystem II at a resolution of 1.9 Å. *Nature* **473**, 55–60 (2011).
14. Hankamer, B., Barber, J. & Boekema, E. J. Structure And Membrane Organization

- Of Photosystem II In Green Plants. *Annu. Rev. Plant Physiol. Plant Mol. Biol.* **48**, 641–671 (1997).
15. Melis, A. Photosystem-II damage and repair cycle in chloroplasts: what modulates the rate of photodamage in vivo? *Trends Plant Sci.* **4**, 130–135 (1999).
 16. Dekker, J. P. & Boekema, E. J. Supramolecular organization of thylakoid membrane proteins in green plants. *Biochim. Biophys. Acta* **1706**, 12–39 (2005).
 17. Lee, C.-I., Lakshmi, K. V & Brudvig, G. W. Probing the Functional Role of Ca²⁺ in the Oxygen-Evolving Complex of Photosystem II by Metal Ion Inhibition†. *Biochemistry* **46**, 3211–3223 (2007).
 18. Kelley, P. M. & Izawa, S. The role of chloride ion in Photosystem II I. Effects of chloride ion on Photosystem II electron transport and on hydroxylamine inhibition. *Biochim. Biophys. Acta - Bioenerg.* **502**, 198–210 (1978).
 19. Rivalta, I. *et al.* Structural-functional role of chloride in photosystem II. *Biochemistry* **50**, 6312–6315 (2011).
 20. Pérez-Navarro, M., Neese, F., Lubitz, W., Pantazis, D. A. & Cox, N. Recent developments in biological water oxidation. *Curr. Opin. Chem. Biol.* **31**, 113–119 (2016).
 21. Najafpour, M. M. *et al.* Manganese Compounds as Water-Oxidizing Catalysts: From the Natural Water-Oxidizing Complex to Nanosized Manganese Oxide Structures. *Chem. Rev.* **116**, 2886–2936 (2016).
 22. Caffarri, S., Croce, R., Breton, J. & Bassi, R. The Major Antenna Complex of Photosystem II Has a Xanthophyll Binding Site Not Involved in Light Harvesting. *J. Biol. Chem.* **276**, 35924–35933 (2001).
 23. Bassi, R. & Dainese, P. A supramolecular light-harvesting complex from chloroplast photosystem-II membranes. *Eur. J. Biochem.* **204**, 317–326 (1992).
 24. Armond, P. A., Staehelin, L. A. & Arntzen, C. J. Spatial relationship of photosystem I, photosystem II, and the light-harvesting complex in chloroplast membranes. *J. Cell Biol.* **73**, 400 LP – 418 (1977).
 25. Croce, R. & van Amerongen, H. Natural strategies for photosynthetic light harvesting. *Nat. Chem. Biol.* **10**, 492 (2014).

Chapter 1

26. Johnson, M. P. *et al.* Photoprotective Energy Dissipation Involves the Reorganization of Photosystem II Light-Harvesting Complexes in the Grana Membranes of Spinach Chloroplasts. *Plant Cell* **23**, 1468 LP – 1479 (2011).
27. Standfuss, J., Terwisscha van Scheltinga, A. C., Lamborghini, M. & Kühlbrandt, W. Mechanisms of photoprotection and nonphotochemical quenching in pea light-harvesting complex at 2.5 Å resolution. *EMBO J.* **24**, 919–28 (2005).
28. Horton, P. Optimization of light harvesting and photoprotection: molecular mechanisms and physiological consequences. *Philos. Trans. R. Soc. B Biol. Sci.* **367**, 3455–3465 (2012).
29. Ruban, A. V & Horton, P. Regulation of Non-Photochemical Quenching of Chlorophyll Fluorescence in Plants. *Funct. Plant Biol.* **22**, 221–230 (1995).
30. Ballottari, M., Girardon, J., Dall’Osto, L. & Bassi, R. Evolution and functional properties of Photosystem II light harvesting complexes in eukaryotes. *Biochim. Biophys. Acta - Bioenerg.* **1817**, 143–157 (2012).
31. Niyogi, K. K. & Truong, T. B. Evolution of flexible non-photochemical quenching mechanisms that regulate light harvesting in oxygenic photosynthesis. *Curr. Opin. Plant Biol.* **16**, 307–314 (2013).
32. Bode, S., Quentmeier, C. C., Liao, P.-N., Barros, T. & Walla, P. J. Xanthophyll-cycle dependence of the energy transfer between carotenoid dark states and chlorophylls in NPQ mutants of living plants and in LHC II. *Chem. Phys. Lett.* **450**, 379–385 (2008).
33. Wasser, I. M., de Vries, S., Moënné-Loccoz, P., Schröder, I. & Karlin, K. D. Nitric Oxide in Biological Denitrification: Fe/Cu Metalloenzyme and Metal Complex NO_x Redox Chemistry. *Chem. Rev.* **102**, 1201–1234 (2002).
34. Jung, C., Vries, S. de & Schünemann, V. Spectroscopic characterization of cytochrome P450 Compound I. *Arch. Biochem. Biophys.* **507**, 44–55 (2011).
35. de Vries, S. Freeze-Quench Kinetics. in *Encyclopedia of Inorganic Chemistry* (John Wiley & Sons, Ltd, 2006). doi:10.1002/0470862106.ia340
36. Kim, S. H., Perera, R., Hager, L. P., Dawson, J. H. & Hoffman, B. M. Rapid Freeze-Quench ENDOR Study of Chloroperoxidase Compound I: The Site of the

- Radical. *J. Am. Chem. Soc.* **128**, 5598–5599 (2006).
37. Jung, C., Schünemann, V. & Lendzian, F. Freeze-quenched iron-oxo intermediates in cytochromes P450. *Biochem. Biophys. Res. Commun.* **338**, 355–364 (2005).
 38. Wålander, O., Zetterqvist, Ö. & Engström, L. Intermediary Phosphorylation of Bovine Liver Nucleoside Diphosphate Kinase: Studies With A Rapid Mixing Technique . *J. Biol. Chem.* **244**, 1060–1064 (1969).
 39. Ballou, D. P. & Palmer, G. A. Practical rapid quenching instrument for the study of reaction mechanisms by electron paramagnetic resonance spectroscopy. *Anal. Chem.* **46**, 1248–1253 (1974).
 40. Palmer, G. & Beinert, H. *Rapid Mixing and Sampling Techniques in Biochemistry. Rapid Mixing and Sampling Techniques in Biochemistry* (Elsevier, 1964). doi:10.1016/B978-1-4832-3260-7.50030-5
 41. Lymn, R. W., Gibson, G. H. & Hanacek, J. A Chemical-Stop Rapid Flow Apparatus. *Rev. Sci. Instrum.* **42**, (1971).
 42. Bray, R. C. Sudden freezing as a technique for the study of rapid reactions. *Biochem. J.* **81**, 189–195 (1961).
 43. Hansen, R. E. & Beinert, H. Syringe Ram for a Rapid-Freeze Sampling Instrument. *Anal. Chem.* **38**, 484–487 (1966).
 44. Cherepanov, A. V & De Vries, S. Microsecond freeze-hyperquenching: development of a new ultrafast micro-mixing and sampling technology and application to enzyme catalysis. *Biochim. Biophys. Acta* **1656**, 1–31 (2004).
 45. Andrew, E. R., Bradbury, A. & Eades, R. G. Nuclear Magnetic Resonance Spectra from a Crystal rotated at High Speed. *Nature* **182**, 1659–1659 (1958).
 46. Lowe, I. J. Free Induction Decays of Rotating Solids. *Phys. Rev. Lett.* **2**, 285–287 (1959).
 47. Schaefer, J. & Stejskal, E. O. Carbon-13 nuclear magnetic resonance of polymers spinning at the magic angle. *J. Am. Chem. Soc.* **98**, 1031–1032 (1976).
 48. Pines, A. Proton-enhanced NMR of dilute spins in solids. *J. Chem. Phys.* **59**, 569 (1973).
 49. Hartmann, S. R. & Hahn, E. L. Nuclear Double Resonance in the Rotating Frame.

Chapter 1

- Phys. Rev.* **128**, 2042–2053 (1962).
50. Lee, M. & Goldburg, W. I. Nuclear-Magnetic-Resonance Line Narrowing by a Rotating rf Field. *Phys. Rev.* **140**, A1261–A1271 (1965).
51. van Rossum, B.-J. *et al.* Multidimensional CP-MAS ¹³C NMR of uniformly enriched chlorophyll. *Spectrochim. Acta Part A Mol. Biomol. Spectrosc.* **54**, 1167–1176 (1998).

Design of a novel device enabling freeze-quench trapping of laser flash activated Photosystem II intermediates.

A three-flash flow cell was designed to enable the study of single or multiple flash activated photochemical reactions. The performance of the device was tested with Photosystem II, in order to study transient intermediates in the mechanism of water oxidation by the manganese cluster. The novel methodology of flash flow RFQ-EPR allows rapid freeze quenching after flash activation followed by spectroscopic measurements, for example by EPR. The current setup consists of three 680 nm diode lasers as light sources, capable of delivering a maximum of three sequential flashes of 10 μ s each, which drive Photosystem II through the Kok cycle as evidenced from the appearance, disappearance and subsequent reappearance of EPR signals associated with intermediates with specific Mn-multiline EPR spectra. The dead time, which is the time between the last flash and hyperquenching of the sample by freezing using liquid isopentane at 140K as the quenching medium, is 2 ± 0.3 ms. The two interconvertible states of S_2^+ which originates from the spin ground state of manganese cluster $S=1/2, 5/2$ are produced at $g=2$ and $g=4.1$ in X band EPR by the flash RFQ method. The conversion efficiency by this method in transitions from S_1^n to S_2^+ is 100%, from S_2^+ to S_3^+ it is 75% and from S_3^+ to S_0^n a conversion efficiency of 60% is achieved.

2.1. Introduction

Photosystem (PS) II is the water splitting multi-subunit protein complex in thylakoid membranes of plants, algae and cyanobacteria¹⁻⁵. PS II carries out light-driven oxidation of two water molecules to form molecular oxygen (O_2)³. Upon flash activation of the PSII reaction center chlorophyll P680, charge separation occurs that generates one oxidizing and one reducing equivalent. The electron is transferred to pheophytin, then to the primary electron acceptor quinone Q_A , and finally to the secondary electron acceptor Q_B . After a second flash, Q_B is doubly reduced and protonated to form Q_BH_2 , which leaves the binding site and is replaced by another acceptor molecule from the Q_B pool. The oxidized primary donor Chl P680 is reduced by an electron from the secondary donor Tyrosine161 from the D1 polypeptide, Y_Z , which is oxidized to the neutral tyrosine radical (Y_Z^*)^{4,6,7}. The Y_Z^* is reduced by one electron from the water oxidizing complex in every charge separation cycle. The Y_Z^* serves as a mediator that decouples the proton transfer from the electron transfer in the catalytic unit⁸. The water oxidation complex consists of a Mn_4Ca cluster that can accumulate a maximum of four positive charges upon which molecular oxygen is released from two water molecules and 4 H^+ are ejected into the lumen^{2,7,8}.

In natural photosynthesis, the water oxidation happens in a cyclical process that contains 9 intermediates and transition states as shown in figure 1a⁹. $S_i^{+/n}$ can represent the one of the intermediate or transition state. Here subscript 'i' indicate the number of oxidation equivalents which are accumulated at water oxidation complex and the superscript indicate the charge of the PS II with respect to the dark stable S_1^n state (n, neutral and +, positive)

The water oxidation cycle in Figure 1 proceeds along a reaction coordinate with decoupled proton transfer and electron transfer steps with four intermediates and five transition states⁹. Although proton transfer and electron transfer alternate during the cycle, the charge state of the water oxidation cluster, which is neutral in the (S_1^n) dark stable intermediate, changes to +1 after the first flash (S_2^+) and remains positive until water oxidation takes place that reverts the cluster to its neutral form. Figure 1.b. shows a square diagram for proton transfer and electron transfer for the cycle in (a). The horizontal

reaction steps indicate proton transfers and vertical reaction steps are for electron transfer. Solid circles indicate stable intermediates and dashed circles depict the transition states according to Dau et al⁹. The steps along intermediates and transition states for the reaction coordinate in PS II are shown with thick arrows. The dashed diagonal lines indicate +1 and neutral isocharge sequences of intermediates. The dark stable intermediate S_1^n is on the neutral isocharge diagonal, and the water oxidation cluster moves over to the +1 isocharge diagonal and the S_2^+ intermediate with the first flash. After three flashes there is an effective mismatch between intermediates and transition states, and the system, which is in the S_3^+ intermediate moves over from +1 isocharge intermediates to neutral intermediates by losing two protons and one electron end up in the S_0^n neutral intermediate. The effective mismatch is resolved in the transition from S_4^+ to S_0^+ which are both transition states and are shown together on the reaction coordinate in the square diagram.

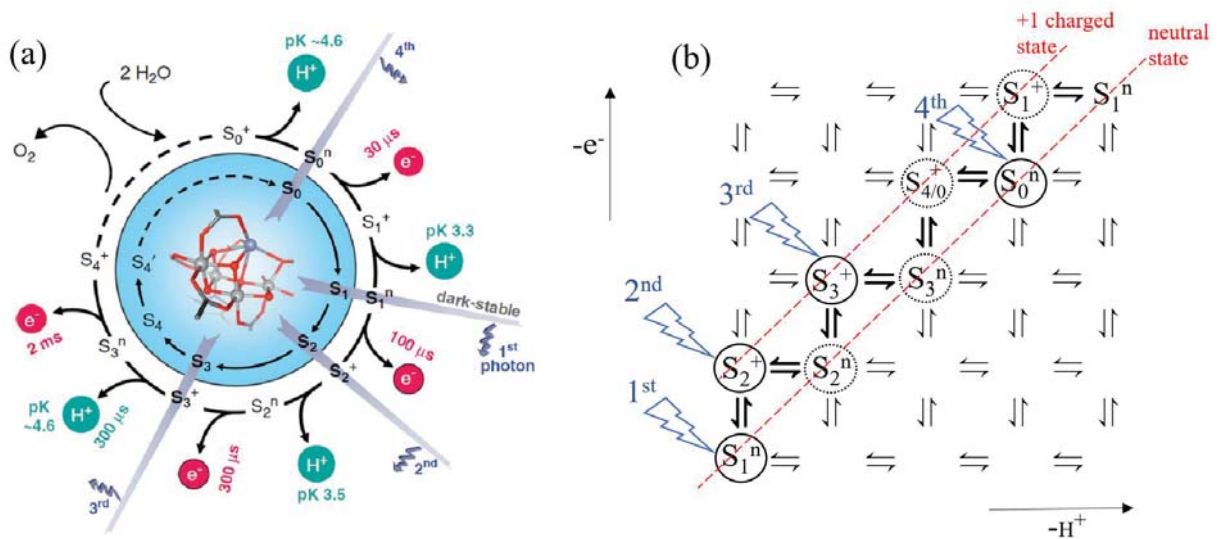


Figure 1. (a) Water oxidation cycle in PS II and (b) square diagram for proton and electron transfer steps. Four states, S_1^n , S_2^+ , S_3^+ and S_0^n , are stable intermediates on short time scales, while (S_2^n , S_3^+ , S_3^n , S_4^+ and S_0^+) are the transition states⁹. The states S_2^+ , S_3^+ are on the diagonal with +1 charge state and S_1^n , S_0^n are on the diagonal with neutral states.

Chapter 2

EPR has proven to be invaluable to characterize PSII, capable of detecting differences between signals of the Mn₄Ca cluster in its different S_i⁺ⁿ states. The total spin of the states S₂⁺, S₀ⁿ are $S_{tot} = \frac{1}{2}$ ^{10,11}. These are detectable by normal mode EPR and characterized in particular by multiline EPR signals at $g = 2$ with an average Mn-hyperfine splitting of ~ 90 Gauss¹²⁻¹⁵. RFQ is extremely useful in trapping transient intermediates formed in biological enzymatic reactions, and the subsequent characterization by various spectroscopic methods including EPR, Mössbauer and Resonance Raman spectroscopy¹⁶⁻²¹. A flash-freeze approach has been used by Dau et al to study structural changes of the Mn complex during the water oxidation cycle by XAFS^{22,23}. It is presently not possible, however, to trap PSII intermediate states by rapid freeze-quenching (RFQ) for the study of the Mn₄Ca cluster by EPR. By the combination of RFQ and a newly designed three-flash flow cell we offer the prospect to study the transient kinetics of the Mn₄Ca-cluster in Photosystem II. The developed technique is in fact applicable to the study of a wide variety of photochemical reactions in combination with a wide array of spectroscopic methods.

2.2. Materials and Methods

2.2.1. Preparation of Photosystem II membrane particles

Oxygen evolving PSII membrane particles were prepared from spinach following a method described by Berthold et al. with a modification of the procedure by Schiller et al^{24,25}. The preparation was performed in the dark or under dim green light at approximately 4°C. Fresh spinach leaves were washed in ice cold water, destemmed and grinded in a blender for 20 seconds, in a medium that contained 0.4M sucrose, 0.4M NaCl, 35mM HEPES (pH 7.5), 4mM MgCl₂, 1mM EDTA, 5mM ascorbic acid and 2 g/l BSA. The suspension was filtered through cheesecloth and centrifuged for 6 min at 5000×g. The chloroplast pellet was resuspended in 25mM HEPES (pH 7.5), 150 mM NaCl, 8mM MgCl₂ and centrifuged for 10 min at 5000×g. The pellet consists of thylakoid membranes and was diluted to a suspension of 2.5 mg Chl/ml with a buffer containing 1M glycine-betaine, 15mM NaCl, 10mM MgCl₂ and 25mM HEPES (pH 6). The suspension

was further diluted, with 25% Triton-X100 (w/v) solution, to give a final Triton concentration of 5% (v/v) with a final concentration of 2 mg Chl/ml and was incubated in the dark with slow stirring for 25 min²⁶. After incubation the suspension was centrifuged for 3 min at 1000×g to remove the starch, followed by centrifugation for 30 min at 48000×g at 4°C. The dark green part of the pellet was subjected to two or three resuspension and centrifugation steps until the white starch spot on the bottom of the pellet was removed completely. The washed Photosystem II particles were stored in final buffer containing 400mM sucrose, 1M glycine-betaine, 30mM NaCl, 5mM MgCl₂, 5mM CaCl₂ and 50mM MES (pH 6) and stored at -80°C in aliquots of 0.75 ml at 10 mg Chl/ml.

Oxygen evolution activity of Photosystem II membrane particles was measured polarographically with a Clark electrode in an assay buffer containing 400mM sucrose, 1M glycine betaine, 30mM NaCl, 5mM MgCl₂ and 50mM MES (pH 6) using saturating light (1200 W/m²). Exogenous artificial electron acceptors, 5mM K₃[Fe(CN)₆] and 0.3mM PPBQ from a freshly prepared stock of 250mM in water and 15mM in DMSO, respectively, were used²⁷. PS II membrane particles were used that had oxygen evolution rates of 300-400 μmol O₂ (mg Chl h)⁻¹.

2.2.2. EPR experiments

X-Band EPR spectra were collected in normal mode at 10K using an ECS106 spectrometer (Bruker) equipped with a home built cryostat²⁸. Measuring conditions were 9.45 GHz, 20 G modulation amplitude, 20 mW microwave power and the scan time was 3 minutes.

2.2.3. Rapid Freeze Quenching

RFQ was performed in a quartz EPR sample tube connected to a funnel with a flexible plastic tube and immersed in isopentane which is cooled to 140 K by slow mixing of liquid N₂ to it as described by Cherepanov et al¹⁷. The excess isopentane removed and EPR tubes were frozen and stored in liquid N₂ until the EPR experiments were performed.

Chapter 2

Three Red diode lasers each provides 800 mW output power, 105 μm fiber core diameter, peak output at a fixed wavelength of 678 nm (BWT Beijing LTD, China) served as light sources. The PEEK tube and capillaries are connected by Micro Tight adapters (Upchurch Scientific). HPLC-type solvent delivery pump (Waters Inc. Type 515) with operational pressures ranging from 0-6000 psi. The experiments were carried out in complete darkness by using EyeClops night vision goggles (Jacks Pacific Inc. California, USA) which carry an internal infrared light source for vision that does not affect PSII.

2.3. Results and Discussion

2.3.1. The construction of Flash-RFQ setup

The schematics of the Three-Flash Flow Cell for rapid freeze quenching of photo excited Photosystem II is shown in Figure. 2. A major challenge in constructing the setup is to obtain sufficient light intensity to get complete turnover of the sample, which requires a light intensity of $> 2 \text{ mJ/cm}^2$ for every flash²⁹. To achieve this, fluid channels made from PEEK tube of inner diameter 400 μm were connected to transparent fused silica capillaries of inner diameter 100 μm with red diode lasers focused perpendicularly on the fused silica capillary tube by SMA couplers. Every red diode laser of 800 mW produces $\sim 50 \text{ mJ/cm}^2$. With a flow rate of 5 ml/min and 100 μm inner diameter capillary tube, 25 times more light intensity is supplied to the sample than required for the full conversion. The overcapacity compensates for laser and flash-cell fiber coupling losses and for the divergence of the fiber beam that initiates the photochemical reaction. Since the PS II particles are moved at a high flow rate across regions of static continuous illumination by the red lasers, PS II particles are exposed to short flashes of red laser light. At a flow rate of 5 ml/min the PS II particles are exposed to red laser flashes of 10 μs , which avoids double hits³⁰.

The dark period between flashes should be more than 150 ms in order to allow for complete reduction of the quinone acceptor side³¹. Sections of PEEK tubing of 10 cm serve this purpose of establishing dark periods. The PEEK tubings are shown as yellow colored conduits in the 3D representation of the three flash cell at the bottom of Figure 2.

After the third flash the suspension leaves as a jet of 100 μm diameter into a funnel that is connected to an EPR tube that is filled with isopentane at 140 K.

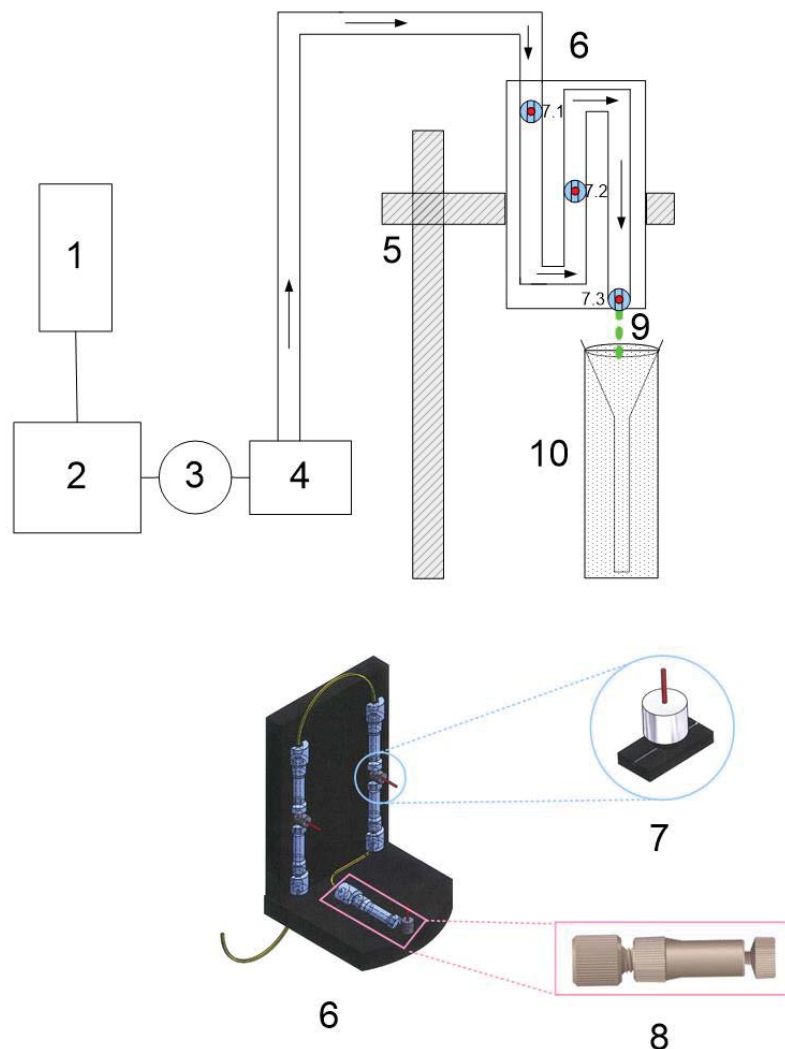


Figure 2. The flash photoexcitation and rapid freeze quenching set up for studying Photosystem II catalytic intermediates. 1) is the buffer bottle. The aqueous buffer serves as the carrier fluid for transporting the sample through the setup. It is made anaerobic by flushing with Ar, which flows continuously when the system is not in operation. 2) HPLC pump for sample injection, 3) Rheodyne injector for transferring aliquots of 0.5 ml sample into a low dead volume 4) through a 0.2 mm filter. 5) Stand to support the three flash cell, 6) The three flash cell with dimensions of 100 mm x 100 mm x 70 mm, 7) SMA-connector to couple a capillary tube with the Red diode laser of 800 mW. 7.1, 7.2, and 7.3 are laser excitation points. 8) Microtight adapters to connect the 100 μm ID fused silica capillary and 400 μm ID PEEK tube, 9) Jet with a diameter of 100 μm and 10) The sample collector funnel is attached to an EPR tube that is immersed in isopentane at 140K.

Chapter 2

The jet speed and the distance between flash and quenching medium determines the time resolution for freeze quenching. The total aging time (τ_a) is the sum of the sample transport time τ_t and the cryofixation time τ_c ¹⁷. The sample transport time is determined by two factors, the linear flow rate and the distance from the third flash cells to the cryomedium as shown in Figure 2. At a linear flow rate of 5 ml/min the sample flow rate equals 10 m/s, and the sample transport time is 1.4 ± 0.2 ms when crossing a distance of 15 mm between the location of the last flash and the quenching medium. The cryofixation time for a jet of 100 μm in isopentane is estimated as 0.6 ± 0.1 ms^{32,33}. So, the sample aging time is 2.0 ± 0.3 ms.

Photosystem II particles were solubilized in a buffer containing 1M betaine. This is critical to stabilize PS II and to enhance free liquid flow in the three-flash flow cell, which reduces the risk of clogging of the microfilter^{25,34,35}. Prior to flash excitation, PSII membrane particles with 9 mg Chl/ml were exposed to ambient light for 5 minutes, followed by a period of 90 minutes dark adaptation, to bring the PS II reaction centers to dark stable intermediates S_1^n . Upon continuous light exposure the PS II reaction centers have an equal distribution over four stable intermediates S_1^n , S_2^+ , S_3^+ and S_0^n . When the light is switched off, the S_2^+ and S_3^+ convert back to S_1^n on a time scale of minutes, while the S_0^n state converts to S_1^n by dark incubation on a longer timescale of 90 minutes, since it requires transferring an electron and reduction of Y_Z ³⁶. After the dark adaptation time, 0.3 mM of artificial electron acceptor PPBQ in DMSO was added to mimic the role of Q_B . PPBQ has similar efficiency in accepting the electron from Q_A ³⁷.

2.3.2. EPR responses of flash excited freeze quenched Photosystem II

The traces in figure 3A indicate the S_2^+ multiline EPR responses that were generated by continuous illumination for 10 minutes at 200 K²⁹. The S_2^+ multiline signal is used as a reference to determine the conversion efficiency of a flash. Trace B depicts the multiline EPR signal from a sample that was first passed through the three-flash flow cell without flashes, and subsequently illuminated for 10 minutes at 200 K. Since the line shapes of the signals in 3A and 3B are the same, Photosystem II remains stable at the high flow rates and pressures generated during the freeze quenching experiment.

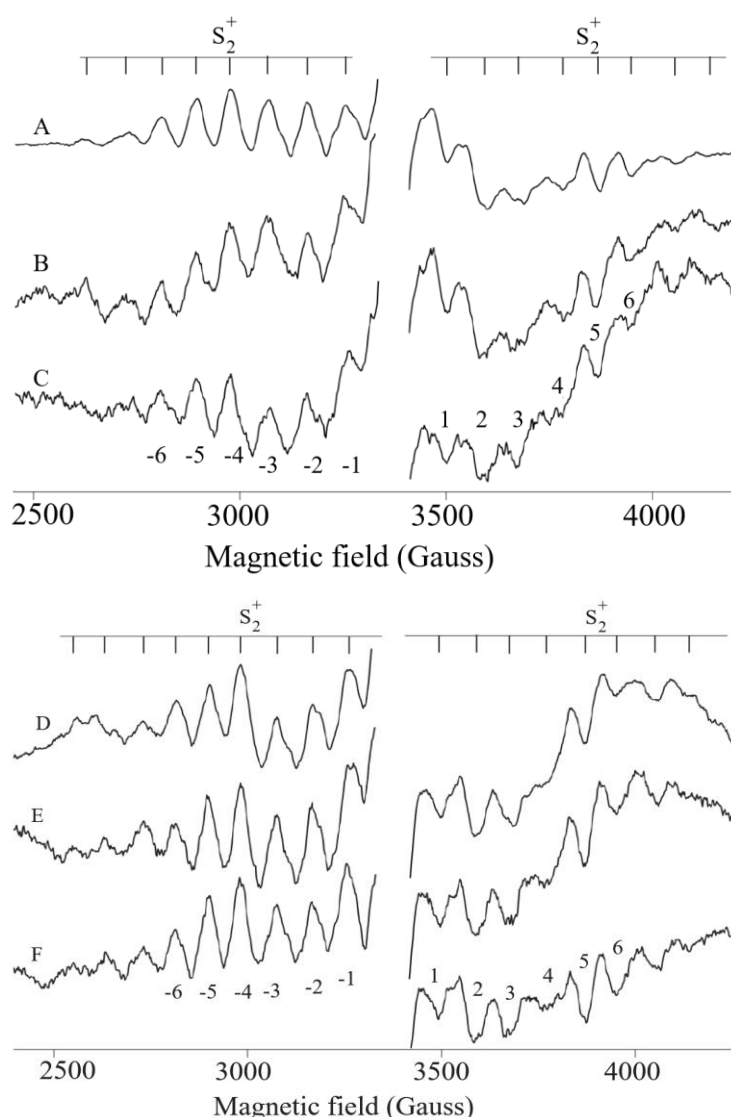


Figure 3. (upper panel) The sample integrity and excitation efficiency can be verified using the S_2^+ multilines signal as a marker. Continuous illumination at 200K of (A) dark adapted reference sample and (B) freeze quenched sample with no flash. (C) Freeze quenched sample after one red laser flash of 10 μ s and aging time of 2 ms. In the lower panel the effect of excitation time on the intensity of the S_2^+ multilines signal is shown. S_2^+ multilines signals were generated by one laser flash of 10 μ s (D), 15 μ s (E) and 25 μ s (F) by adjusting the fluid flow rate to 5, 3.3 and 2 ml/min, respectively. The lines labelled -6 to 6 indicate the S_2^+ multilines peak positions that were used to determine peak heights and relative concentrations.

For comparison, we have also performed some experiments with MHQ using a rotating disk for freezing the sample, which has the advantage of more rapid freezing compared to the RFQ in isopentane. However, it was found that the Mn was released under MHQ conditions due to degradation of PS II, and a free Mn^{2+} signal was observed (Appendix). Trace C in figure 3 is from a sample illuminated by one red laser in the three-flashflow cell freeze quenched.

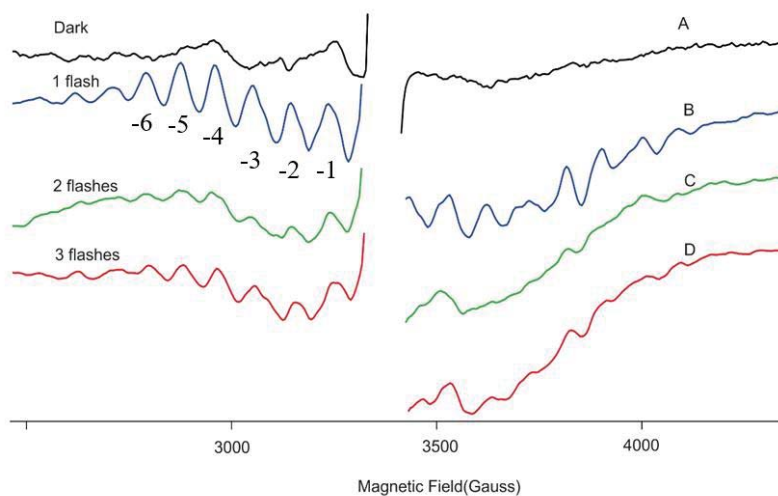


Figure 4. EPR spectra showing the generation of S_2^+ , S_3^+ and S_0^n states by sequential laser flashes followed by freeze-quenching. Trace A, dark signal, traces B, C and D represent the S_2^+ , S_3^+ and S_0^n states respectively, and were after 1, 2 or 3 red laser flashes of 10 μs each. The total aging time, τ_a of each sample is 2 ms and the exhaust jet is freeze quenched with cold isopentane at $T=140\text{K}$. The lines labelled -6 to -1 indicate the S_2^+ multiline peak positions that were used to determine peak heights and relative concentrations.

The normalized intensity of the S_2^+ multiline signal of trace C is nearly equal to trace A and B which indicates complete conversion. The traces D, E and F in figure 3.b. show the S_2^+ multiline signal generated by excitation after one flash with sample illumination times of 10, 15 and 25 μs . These illumination times were achieved by varying the flow rates of 5, 3.3 and 2 ml/min, respectively. Increasing the illumination time of 10, 15 and 25 μs did not alter the average intensity of the peaks, indicating there were very few if any double hits. This confirms the full and clean conversion of S_1^n to S_2^+ in 10 μs . In the case of double hits, the S_2^+ intensity would have decreased as it would have converted to S_3^+ .

The results of multiple flashes are shown in Figure 4. After the sample preparation and the dark period, the sample is in the S_1^n intermediate. The EPR spectra of S_1^n , S_2^+ , S_3^+ and S_0^n were generated by application of 0, 1, 2 or 3 laser flashes, respectively. Trace B in figure 4 shows the multiline signal at $g=2$ with 92 G line spacing, which originates from the conversion into the S_2^+ intermediate state, which has a total spin ($S=1/2$). The figure 5 shows the $g=4.1$ signal with 500 G line width of S_2^+ intermediate state with total spin ($S=5/2$). These two forms are interconvertible at room temperature.^{38,39} The $g=4.1$ signal

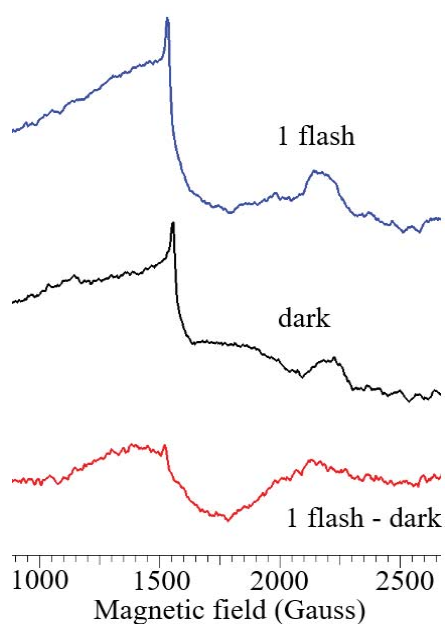


Figure 5. The EPR spectrum of the $g=4.1$ signal of the S_2^+ intermediate (bottom trace) is obtained from the difference between the EPR response after one flash (top trace) and data collected from rapidly freeze quenched sample without flash excitation (middle trace).

overlaps with a strong response from rhombic iron at $g=4.31$. Since the rhombic iron signal is not affected by the flashes, it can be subtracted to reveal the $g=4.1$ response for the S_2^+ intermediate (Figure 5). After two flashes the intensity of the S_2^+ multiline signal pattern had decreased by 75% by partial conversion of the S_2^+ intermediate to the S_3^+ form. The total spin of the S_3^+ state is $S=3$, which does not give a response around $g=2$ in normal mode X-band EPR⁴⁰. After three flashes the strength of the multi-line signal increases (trace D). Studies of the S_0 state have been performed with EPR in the past, and have provided converging evidence for a $g=2$ signal only, *i.e.* without the $g=4.1$ response that is characteristic for the second component of the S_2^+ state (see Appendix, Figure 2A.2)⁴¹. Hence we attribute trace D in figure 4 to partial conversion to the S_0^n state. The total spin of the S_0^n intermediate state is $S=1/2$ and it produces $g=2$ multiline signal⁴¹. The intensity of the $g=2$ signal is 45% of the original S_2^+ multi-line signal (trace

B) and this suggests an approximate 60% conversion by the third flash. Thus the conversion efficiencies from the initial S_1^n state decreases after each flash, from 100% to 75% to 60%, whilst each flash is saturating (Figure 3). Two possible explanations for this decreasing conversion efficiency can be given: 1) the dark time (150 ms) between flashes is too short or 2) the concentration of PPBQ (0.3 mM at 8 – 10 Chl mg/ml) is too low. In both cases this leads to incomplete regeneration of the Q_A^- radical state to Q_A , and the electron acceptor side of PS II is thought to limit the rate for oxygen evolution⁴².

2.4. Conclusion

The results indicate the successful implementation of a new flash-flow RFQ set up to study intermediates in photochemical reactions and its demonstration in resolving PSII intermediates. In its present form the total dead time (τ_a) is calculated at 2 ± 0.3 ms, determined by the jet travelling time 1.4 ± 0.2 ms and freeze quenching time 0.6 ± 0.1 ms. The present set up can deliver up to three flashes. The system is successfully tested for one, two and three flashes to drive the water oxidation by PS II.

2.5. References

1. McEvoy, J. P. & Brudvig, G. W. Water-Splitting Chemistry of Photosystem II. *Chem. Rev.* **106**, 4455–4483 (2006).
2. Dekker, J. & Van Grondelle, R. Primary charge separation in Photosystem II. *Off. J. Int. Soc. Photosynth. Res.* **63**, 195–208 (2000).
3. Nugent, J. H. A., Rich, A. M. & Evans, M. C. W. Photosynthetic water oxidation: towards a mechanism. *Biochim. Biophys. Acta - Bioenerg.* **1503**, 138–146 (2001).
4. Hansson, O. & Wydrzynski, T. Current perceptions of Photosystem II. *Photosynth. Res.* **23**, 131–162 (1990).
5. Guskov, A. *et al.* Cyanobacterial photosystem II at 2.9-Å resolution and the role of quinones, lipids, channels and chloride. *Nat. Struct. & Mol. Biol.* **16**, 334 (2009).
6. Nugent, J. H. A. Oxygenic Photosynthesis. *Eur. J. Biochem.* **237**, 519–531 (1996).
7. Styring, S., Sjöholm, J. & Mamedov, F. Two tyrosines that changed the world: Interfacing the oxidizing power of photochemistry to water splitting in photosystem II. *Biochim. Biophys. Acta - Bioenerg.* **1817**, 76–87 (2012).
8. Dau, H. & Haumann, M. Eight steps preceding O–O bond formation in oxygenic photosynthesis—A basic reaction cycle of the Photosystem II manganese complex. *Biochim. Biophys. Acta - Bioenerg.* **1767**, 472–483 (2007).
9. Dau, H., Zaharieva, I. & Haumann, M. Recent developments in research on water oxidation by photosystem II. *Curr. Opin. Chem. Biol.* **16**, 3–10 (2012).
10. Bonvoisin, J., Blondin, G., Girerd, J.-J. & Zimmermann, J.-L. Theoretical study of the multiline EPR signal from the S2 state of the oxygen evolving complex of photosystem II: Evidence for a magnetic tetramer. *Biophys. J.* **61**, 1076–1086 (1992).
11. Kulik, L. V, Epel, B., Lubitz, W. & Messinger, J. 55Mn Pulse ENDOR at 34 GHz of the S0 and S2 States of the Oxygen-Evolving Complex in Photosystem II. *J. Am. Chem. Soc.* **127**, 2392–2393 (2005).

Chapter 2

12. Dismukes, G. C. & Siderer, Y. Intermediates of a polynuclear manganese center involved in photosynthetic oxidation of water. *Proc. Natl. Acad. Sci.* **78**, 274 LP – 278 (1981).
13. Dismukes, G. C. & Siderer, Y. EPR spectroscopic observations of a manganese center associated with water oxidation in spinach chloroplasts. *FEBS Lett.* **121**, 78–80 (1980).
14. Zheng, M. & Dismukes, G. C. Orbital Configuration of the Valence Electrons, Ligand Field Symmetry, and Manganese Oxidation States of the Photosynthetic Water Oxidizing Complex: Analysis of the S₂ State Multiline EPR Signals. *Inorg. Chem.* **35**, 3307–3319 (1996).
15. Ioannidis, N. & Petrouleas, V. Electron Paramagnetic Resonance Signals from the S₃ State of the Oxygen-Evolving Complex. A Broadened Radical Signal Induced by Low-Temperature Near-Infrared Light Illumination. *Biochemistry* **39**, 5246–5254 (2000).
16. Kim, S. H., Perera, R., Hager, L. P., Dawson, J. H. & Hoffman, B. M. Rapid Freeze-Quench ENDOR Study of Chloroperoxidase Compound I: The Site of the Radical. *J. Am. Chem. Soc.* **128**, 5598–5599 (2006).
17. Cherepanov, A. V & de Vries, S. Microsecond freeze-hyperquenching: development of a new ultrafast micro-mixing and sampling technology and application to enzyme catalysis. *Biochim. Biophys. Acta - Bioenerg.* **1656**, 1–31 (2004).
18. Lu, S., Wiertz, F. G. M., de Vries, S. & Moënne-Loccoz, P. Resonance Raman characterization of a high-spin six-coordinate iron(III) intermediate in metmyoglobin–azido complex formation trapped by microsecond freeze-hyperquenching (MHQ). *J. Raman Spectrosc.* **36**, 359–362 (2005).
19. Wiertz, F. G. M., Richter, O.-M. H., Ludwig, B. & Vries, S. de. Kinetic Resolution of a Tryptophan-radical Intermediate in the Reaction Cycle of *Paracoccus denitrificans* Cytochrome c Oxidase. *J. Biol. Chem.* **282**, 31580–31591 (2007).
20. Ballou, D. P. & Palmer, G. A. Practical rapid quenching instrument for the study of reaction mechanisms by electron paramagnetic resonance spectroscopy. *Anal. Chem.* **46**, 1248–1253 (1974).

21. de Vries, S. Freeze-Quench Kinetics. in *Encyclopedia of Inorganic Chemistry* (John Wiley & Sons, Ltd, 2006). doi:10.1002/0470862106.ia340
22. Dau, H. & Haumann, M. X-ray absorption spectroscopy to watch catalysis by metalloenzymes: status and perspectives discussed for the water-splitting manganese complex of photosynthesis. *J. Synchrotron Radiat.* **10**, 76–85 (2003).
23. Haumann, M., Müller, C., Liebisch, P., Neisius, T. & Dau, H. A novel BioXAS technique with sub-millisecond time resolution to track oxidation state and structural changes at biological metal centers. *J. Synchrotron Radiat.* **12**, 35–44 (2005).
24. Berthold, D. A., Babcock, G. T. & Yocum, C. F. A highly resolved, oxygen-evolving photosystem II preparation from spinach thylakoid membranes. *FEBS Lett.* **134**, 231–234 (1981).
25. Schiller, H. & Dau, H. Preparation protocols for high-activity photosystem II membrane particles of green algae and higher plants, pH dependence of oxygen evolution and comparison of the S₂-state multiline signal by X-band EPR spectroscopy. *J. Photochem. Photobiol. B.* **55**, 138–144 (2000).
26. Dau, H. *et al.* Structural Consequences of Ammonia Binding to the Manganese Center of the Photosynthetic Oxygen-Evolving Complex: An X-ray Absorption Spectroscopy Study of Isotropic and Oriented Photosystem II Particles. *Biochemistry* **34**, 5274–5287 (1995).
27. Bao, H., Zhang, C., Ren, Y. & Zhao, J. Low-temperature electron transfer suggests two types of QA in intact photosystem II. *Biochim. Biophys. Acta - Bioenerg.* **1797**, 339–346 (2010).
28. von Wachenfeldt, C., de Vries, S. & van der Oost, J. The CuA site of the caa 3-type oxidase of *Bacillus subtilis* is a mixed-valence binuclear copper centre. *FEBS Lett.* **340**, 109–113 (1994).
29. Joliot, P., Joliot, A., Bouges, B. & Barbieri, G. Studies Of System Ii Photocenters By Comparative Measurements Of Luminescence, Fluorescence, And Oxygen Emission*. *Photochem. Photobiol.* **14**, 287–305 (1971).

Chapter 2

30. Jursinic, P. Investigation of double turnovers in Photosystem II charge separation and oxygen evolution with excitation flashes of different duration. *Biochim. Biophys. Acta - Bioenerg.* **635**, 38–52 (1981).
31. Lavergne, J. Mode of action of 3-(3,4-dichlorophenyl)-1,1-dimethylurea. Evidence that the inhibitor competes with plastoquinone for binding to a common site on the acceptor side of Photosystem II. *Biochim. Biophys. Acta - Bioenerg.* **682**, 345–353 (1982).
32. Palmer, G., Bray, R. C. & Beinert, H. Direct Studies On The Electron Transfer Sequence In Xanthine Oxidase By Electron Paramagnetic Resonance Spectroscopy. I. Techniques And Description Of Spectra. *J. Biol. Chem.* **239**, 2657–66 (1964).
33. De Vries, S., Albracht, S. P. J., Berden, J. A. & Slater, E. C. The pathway of electrons through QH₂:cytochrome c oxidoreductase studied by pre-steady-state kinetics. *Biochim. Biophys. Acta - Bioenerg.* **681**, 41–53 (1982).
34. Chen, T. H. H. & Murata, N. Glycinebetaine: an effective protectant against abiotic stress in plants. *Trends Plant Sci.* **13**, 499–505 (2008).
35. Papageorgiou, G. C. & Murata, N. The unusually strong stabilizing effects of glycine betaine on the structure and function of the oxygen-evolving Photosystem II complex. *Photosynth. Res.* **44**, 243–252 (1995).
36. Styring, S. & Rutherford, A. W. In the oxygen-evolving complex of photosystem II the S₀ state is oxidized to the S₁ state by D⁺ (signal II_{slow}). *Biochemistry* **26**, 2401–2405 (1987).
37. Lee, C.-I., Lakshmi, K. V & Brudvig, G. W. Probing the Functional Role of Ca²⁺ in the Oxygen-Evolving Complex of Photosystem II by Metal Ion Inhibition†. *Biochemistry* **46**, 3211–3223 (2007).
38. Haddy, A., Lakshmi, K. V, Brudvig, G. W. & Frank, H. A. Q-Band EPR of the S₂ State of Photosystem II Confirms an S=5/2 Origin of the X-Band g=4.1 Signal. *Biophys. J.* **87**, 2885–2896 (2004).
39. Krewald, V. *et al.* Metal oxidation states in biological water splitting. *Chem. Sci.* **6**,

- 1676–1695 (2015).
40. Boussac, A., Sugiura, M., Rutherford, A. W. & Dorlet, P. Complete EPR Spectrum of the S3-State of the Oxygen-Evolving Photosystem II. *J. Am. Chem. Soc.* **131**, 5050–5051 (2009).
 41. Geijer, P., Deák, Z. & Styring, S. Proton Equilibria in the Manganese Cluster of Photosystem II Control the Intensities of the S0 and S2 State $g \approx 2$ Electron Paramagnetic Resonance Signals. *Biochemistry* **39**, 6763–6772 (2000).
 42. Shevela, D. & Messinger, J. Probing the turnover efficiency of photosystem II membrane fragments with different electron acceptors. *Biochim. Biophys. Acta - Bioenerg.* **1817**, 1208–1212 (2012).

2.5. Appendix

Figure 2A.1: Free Mn^{2+} EPR signal of degraded Photosystem II under MHQ condition.

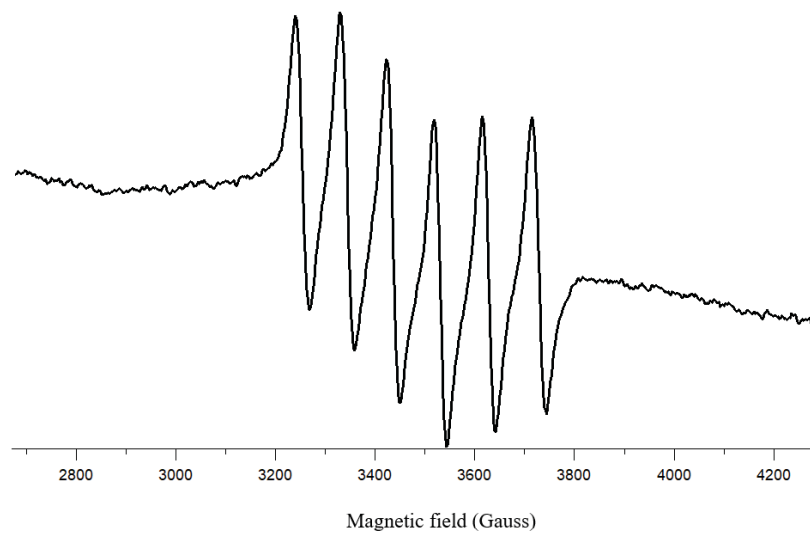
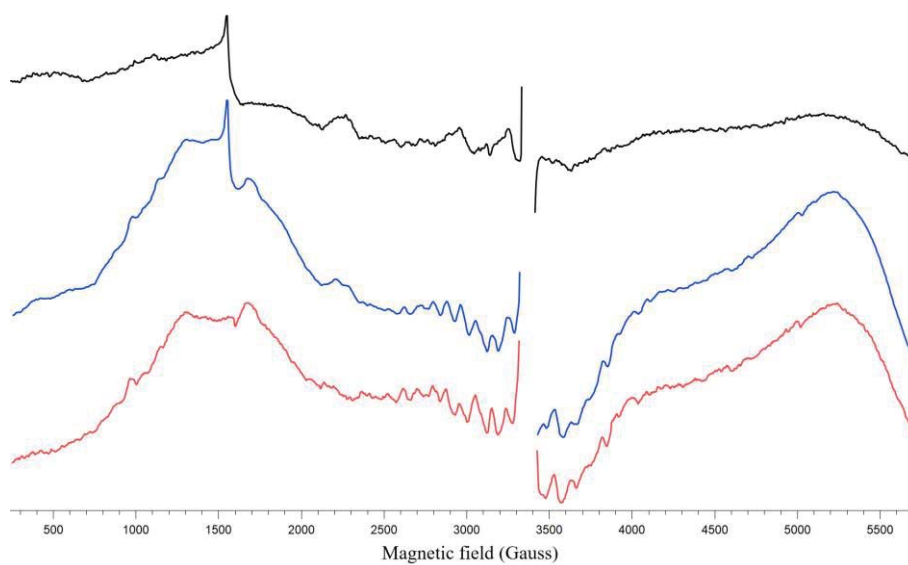


Figure 2A.2 The EPR spectrum of the S_0^n intermediate (bottom trace) is obtained from the difference between the EPR response after three flashes (middle trace) and data collected from rapidly freeze quenched sample without flash excitation (top trace).



Insights in the photoprotective switch of the Major Light-Harvesting Complex II (LHCII): A preserved core of arginine-glutamate interlocked helices complemented by adjustable loops.

Light-harvesting antennae of the LHC family form transmembrane three-helix bundles of which two helices are interlocked by conserved arginine-glutamate (Arg-Glu) ion pairs that form ligation sites for chlorophylls (Chls). The antenna proteins of photosystem II have an intriguing dual function: in excess light they can switch their conformation from a light-harvesting into a photoprotective state, in which the excess and harmful excitation energies are safely dissipated as heat. Here we applied Magic-Angle Spinning (MAS) NMR and selective Arg isotope enrichment as a non-invasive method to analyze the Arg structures of the major light-harvesting complex II (LHCII). The conformations of the Arg residues that interlock helix A and B appear to be preserved in the light-harvesting and photoprotective state. Several Arg residues have very downfield shifted proton NMR responses, indicating that they stabilize the complex by strong hydrogen bonds. For the Arg C_{α} chemical shifts, differences are observed between LHCII in the active, light-harvesting and in the photoprotective, quenched state. These differences are attributed to a conformational change of the Arg residue in the stromal loop region. We conclude that the interlocked helices of LHCII form a rigid core. Consequently, the LHCII conformational switch does not involve changes in A/B helix tilting but likely involves rearrangements of the loops and helical segments close to the stromal and lumen ends.

Chapter 3

This chapter has been published as:

“Insights in the photoprotective switch of the Major Light-Harvesting Complex II (LHCII): A preserved core of arginine-glutamate interlocked helices complemented by adjustable loops.” Kiran Sunku, Huub. J. M. de Groot and Anjali Pandit, *The Journal of Biological Chemistry*, **2013**, 288, 19796-19804.

3.1. Introduction

The elementary step in photosynthesis is the capture of solar energy by the light-harvesting antenna. In eukaryotic organisms, this step is performed by a family of pigment-binding proteins called Light Harvesting Complexes (LHC) that absorb sunlight and transfer the excitation energy towards the reaction centers, where charge separation takes place¹. The Lhcb antenna proteins of higher plants and moss and Lhcbm antenna proteins of LHC complexes in green algae contain three membrane-spanning helices A, B and C and their tertiary structure is typified by two crossing A/B helices interconnected by Arg-Glu ion-pairs that form ligation sites for Chls.

The most abundant LHC complex in plants and green algae is the major light-harvesting complex II (LHCII), which captures about 50% of all land-bound chlorophylls. The LHCII complex is trimeric and each monomer forms a scaffold for 8 Chl *a* and 6 Chl *b*, 2 luteins (Lut), 1 neoxanthin (Neo) and 1 violaxanthin (Vio) which is reversibly replaced by zeaxanthin (Zea) upon de-epoxidation during the xanthophyll cycle²⁻⁴.

In addition to their light-harvesting function, LHCII complexes are involved in several regulatory mechanisms that balance the incoming excitation energies and prevent photodamage^{1,4-6}. Under high sunlight conditions, the photosynthetic antenna can rapidly switch from light-harvesting into a photoprotective state in which excess light energy is safely dissipated as heat⁷. This photoprotective mechanism is called non-photochemical quenching (NPQ) and protects oxygenic organisms against photooxidative damage. The major component of NPQ, qE, depends on the transmembrane proton gradient ΔpH . In plants, a decrease in luminal pH triggers protonation of PsbS^{8,9} and of LHC complexes in photosystem II¹⁰ and activates the conversion of the LHC-bound xanthophyll cycle carotenoid from Vio to Zea¹¹. In green algae, PsbS is absent, and the NPQ state is triggered by LhcSR; a pigment-binding complex with a short fluorescence lifetime that senses the decrease in luminal pH¹²⁻¹⁴. In algae, LHCII also participates in quenching, in particular the Lhcbm1 component^{15,16}. On a supramolecular scale, a reorganization of the thylakoid membrane takes place in which the LHCII complexes dissociate from photosystem II and self-associate or associate with PsbS¹⁷⁻²⁰. The supramolecular rearrangements, xanthophyll exchange and decrease in luminal pH were proposed to

Chapter 3

promote subtle conformational changes inside the photosystem II light-harvesting proteins, by which altered chromophore configurations create a dissipation channel for the incoming light energy²¹.

To date, the molecular basis for the photophysical process of NPQ is under much debate^{22–28} and it is unclear how the LHC's respond to environmental changes and energy-dissipative channels are formed. The LHCII complexes of plants have been studied extensively and were shown to reversibly switch their conformation between active, unquenched and photoprotective quenched conformational states^{24,29,30}. In the photoprotective state, Chl excitations in LHCII are quenched by Chl-Lut energy transfer²⁴ or by low-lying Chl-Lut excitonic states²³, while also Chl-Chl charge transfer states have been proposed²⁵.

There is a controversy whether the LHCII X-ray structures represent the active or quenched form of the protein^{22,31,32}. LHCII complexes reconstituted in lipid nanodiscs retained their fluorescent state but showed small spectral changes compared to LHCII in detergent micelles³³, suggesting that the protein can adopt slightly different conformations within its active state. The quenched state is associated with a twist in the configuration of the LHCII-bound Neo that may promote conformational changes at the Lut L1 site²⁴. Protonation of specific acidic residues under low luminal pH conditions could trigger conformational changes of the short helix D and the BC loop² and these residues are important for stabilizing the complex at different pH values³⁴. Under NPQ conditions, changes in the thickness of the thylakoid membrane have been observed and it was proposed that LHCII adopts a more condensed structure³⁵.

In this work, we applied MAS-NMR techniques in combination with selective Arg isotope labeling as a non-invasive method to obtain high-resolution structural information of LHCII in its active and photoprotective states. Photosynthetic light-harvesting proteins are accessible for NMR via uniformly or selective isotope enrichment of the photosynthetic organisms³⁶. This way, pigment-protein interactions could be detected in atomic detail inside intact purple-bacterial light-harvesting oligomers^{37–39}. More recently, we performed a MAS-NMR analysis of LHCII from uniformly-¹³C enriched *C. reinhardtii* green algae cells^{40,41}. The *C. reinhardtii* Lhcbm sequences have a high

similarity with Lhcb sequences of higher plants⁴⁰, making *C. reinhardtii* LHCII a suitable *in-vitro* model system for the structural flexibility of plant Lhcb and algae Lhcbm proteins.

Here we analyze LHCII complexes from an Arg-auxotrophic strain of *C. reinhardtii* that was supplied with ¹³C₆-¹⁵N₄ Arg. 1D ¹³C and ¹⁵N CP-MAS and 2D ¹H-¹³C dipolar heteronuclear correlation (HetCor) Arg NMR spectra are presented of LHCII in quenched and unquenched states. The Arg residues that stabilize the interlocked helix pair in LHCII are identified owing to Chl ring current-induced shifts of their NMR responses. We show that these protein sites are preserved in the photoprotective state, confirming a structural view in which the flexible loop regions of the LHCII polypeptides are complemented by a relatively rigid scaffolding of the protein interior⁴².

3.2. Materials and Methods

3.2.1. Isotope enrichment and purification of LHCII trimers

Chlamydomonas reinhardtii strain cc424, an Arg-auxotrophic strain obtained commercially from Chlamy.org (www.chlamy.org) was grown in liquid TAP medium⁴³ with 50 mg/Lt of Arg used⁴⁴. Cells were cultured at room temperature under continuous illumination at 60 μ E flux. Arginine was added separately to the cell cultures and for selective Arg enrichment was substituted by ¹³C₆,¹⁵N₄ Arg purchased from Silantes GmbH. The cells were harvested in mid-log phase by centrifugation (4000 rpm, 6 min, 4 °C) and thylakoids were prepared as described in⁴⁵ with few modifications described in⁴⁶. Thylakoids were separated from other materials on a discontinuous gradient (24000 rpm, 1hr, 4°C) in a TST-41.14 swingout rotor. Thylakoid membranes were washed 2 times, first with 10mM HEPES, pH 7.5, and 5mM EDTA and finally with 10mM HEPES, pH 7.5. Thylakoids were resuspended in solubilization buffer (10mM HEPES, pH 7.5) to a Chl concentration of 1 mg/ml and equal amounts of β -dodecylmaltoside (β -DM) was added to get a final concentration of 0.6% β -DM. The suspension was vortexed for a few seconds and centrifuged (15000 rpm, 10 min, 4°C) to remove unsolubilized material, and the supernatant was loaded on a sucrose density gradient, prepared by 0.65M sucrose, 10 mM tricine, pH 7.8, 0.03% β -DM and ultracentrifuged for 17 hrs at 37000 rpm. The top

Chapter 3

band of the sucrose gradient contained LHCII trimer complexes with more than 90% purity, verified by FPLC.

For obtaining LHCII in its quenched state, isolated LHCII trimers in 0.03% β -DM were dialyzed for 72 hrs against detergent-free buffer. The quenched state of the detergent-depleted LHCII aggregates was verified by low-temperature fluorescence spectroscopy, while the unquenched, light-harvesting state of the LHCII trimers in β -DM was verified by time-resolved fluorescence spectroscopy.

3.2.2 Fluorescence experiments

Steady-state fluorescence excitation and emission spectra were measured with a commercial spectrophotometer (Jobin Yvon, Fluorolog). For 77K fluorescence emission measurements, the samples were diluted in 40% Hepes/ β -DM buffer and 60% glycerol (v/v) and cooled in a nitrogen-bath cryostat to 77K.

Time-resolved fluorescence emission measurements were performed at room temperature with a Streak camera setup. The sample was measured front-face using a 1mm quartz cuvette. To minimize the effects of photodamage, about 10 spectra of maximal 1 minute per scan were acquired. It was verified that within this time period of illumination, no degradation of sample occurred. Excitation pulses of 400 nm (\sim 100 fs) with vertical polarization were generated using a titanium:sapphire laser (Coherent Vitesse) with a regenerative amplifier (Coherent, MIRA seed and RegA), that was used to pump an optical parametric amplifier (Coherent, OPA). The repetition rate was 50 kHz with pulse energies of \sim 0.2 nJ. A tenfold increase or two-fold decrease of the excitation pulse energy did not affect the fluorescence lifetimes, confirming that experiments were performed in the annihilation-free regime. The obtained streak data were analyzed with Glotaran³⁴⁷.

3.2.3. Solid-state NMR experiments

1D ^{13}C and ^{15}N and 2D ^1H - ^{13}C frequency-switched Lee-Goldburg (FLSG) heteronuclear correlation experiments were performed with a Bruker AV-750 spectrometer equipped with a 4-mm triple resonance MAS probe head, using a ^{13}C radio frequency of 188.6 MHz. The temperature was lowered to 220-240 K under slow spinning

of the sample. For the NMR experiments, spinning frequencies of 13 kHz were used. The chemical shift scale was calibrated from a FSLG spectrum of solid tyrosine HCl salt.

3.2.4. Density Functional Theory calculations

DFT calculations were performed in vacuum within the DFT frame work and using the Gaussian 03 package⁴⁸. The BLYP exchange correlation function⁴⁹⁻⁵¹ was applied to produce the NMR chemical shifts^{48,52}. The geometric arrangements of R70, E180 and Chl610 were extracted from the 2BHW crystallographic structure data for pea LHCII³. The phytyl group of the Chl610 was truncated at the ester group and replaced by an H atom. The truncation had no effect on the electronic structure of the porphyrin ring. The geometries were partially optimized, preserving the planar structure of the Chl macrocycle and of the backbone of R70 and E180. The ¹H, ¹³C, ¹⁵N NMR chemical shieldings were calculated by using the gauge-independent atomic orbital (GIAO)⁵³⁻⁵⁶ on the whole complex and subsequently NMR calculations were performed. Both for partial optimization and NMR chemical shift calculations the BLYP/6-311G** basis set was used.

3.3. Results

3.3.1. Fluorescence conditions of LHCII in the detergent-solubilized and aggregated state

LHCII was prepared in its active, light-harvesting state, by solubilizing the LHCII complexes in β -DM buffer. Time-resolved fluorescence experiments on LHCII complexes concentrated in β -DM buffer solution verified that the light-harvesting state of LHCII was retained in highly concentrated form required for the NMR experiments. Figure 3.1 shows the decay-associated spectra (DAS) obtained by a global-analysis fitting of the streak camera images of LHCII concentrated in β -DM solution. The average fluorescence lifetime $\langle\tau_f\rangle$ of this sample is 3.0 ns, and this verifies that the concentrated sample of LHCII in β -DM buffer retained its unquenched state. LHCII aggregates that reflect the photoprotective state of LHCII were produced by dialysis against detergent-free buffer. For the aggregate sample, the fluorescence signal was below the detection limit of the Streak camera setup and its quenched state was verified by a 77K steady-state

fluorescence emission spectrum. Figure 3.2 presents a 77K fluorescence spectrum of LHCII in β -DM buffer (dashed spectrum) and after dialysis against detergent-free buffer (solid spectrum). Significant fluorescence quenching of LHCII aggregates formed upon dialysis is confirmed by the 10 fold decrease and 4 nm red shift of the fluorescence peak at 675 nm, and appearance of an additional fluorescence band at 695 nm, which has been associated with quenching and aggregation of LHCII³⁰.

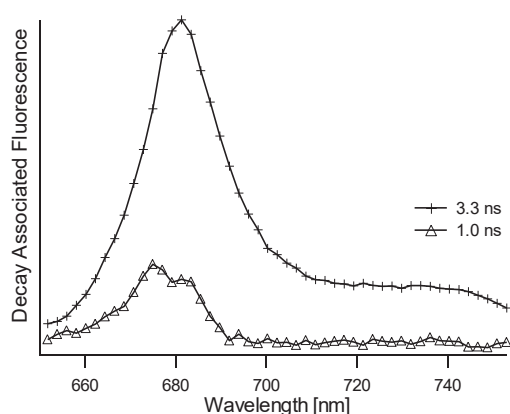


FIGURE 3.1. Decay-associated fluorescence spectra and associated lifetimes of LHCII concentrated in β -DM buffer solution.

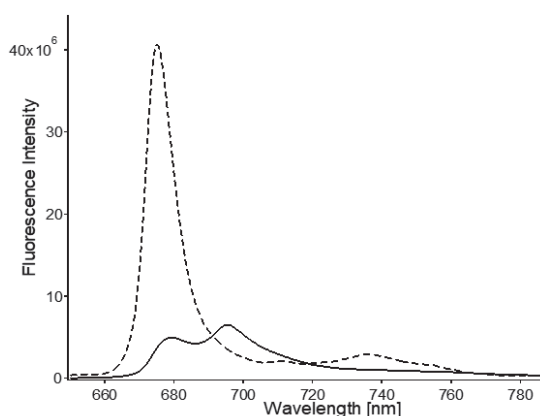


FIGURE 3.2. 77K fluorescence spectra of LHCII: A. LHCII in β -DM buffer (dashed spectrum) and B. LHCII in detergent-free buffer after extensive dialysis for removal of the β -DM (solid spectrum).

3.3.2. Arg NMR responses for LHCII in its active and dissipative state

Figure 3.3 shows the 1D ^{13}C (A) and ^{15}N (B) CP-MAS spectra of quenched (solid) and unquenched (dashed) LHCII. In panel C, the second derivative of the ^{15}N spectra are drawn. The Arg chemical structure is drawn with the spectra in panel A. The natural abundance ^{13}C NMR responses of the β -DM detergent molecules are denoted with asterisks in the ^{13}C spectrum of unquenched LHCII. Selective $^{13}\text{C}_6, ^{15}\text{N}_4$ Arg enrichment of the LHCII samples is confirmed by the characteristic C_ζ Arg peaks around 158 ppm and N_η and N_ϵ responses around ~ 72 and ~ 82 ppm, respectively. Both samples show splitting of NMR responses for the Arg C_ζ , C_δ and C_α and for the N_η and N_ϵ and N atoms.

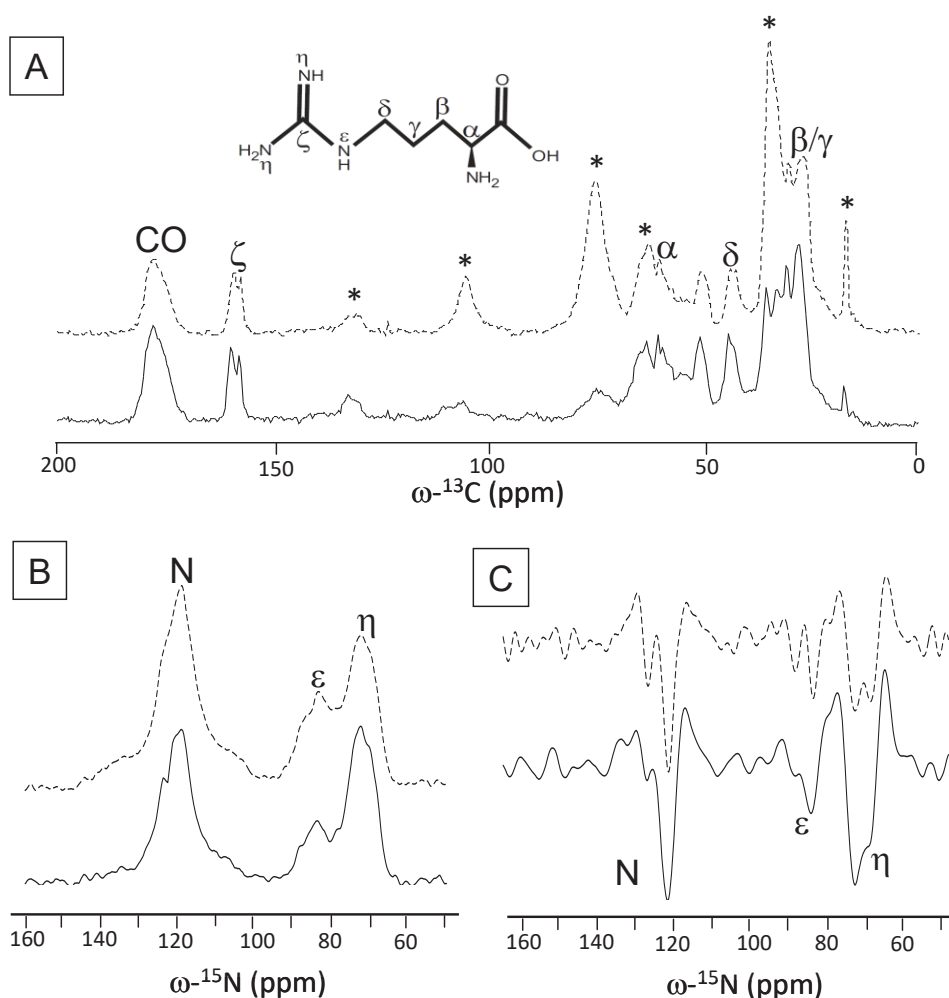


FIGURE 3.3. A: ^{13}C CP-MAS spectra of unquenched (dashed line) and quenched (solid line) LHCII. Detergent peaks in unquenched LHCII are denoted with asterisks. The chemical structure of Arg is also shown. B: ^{15}N CP-MAS spectra of unquenched (dashed line) and quenched (solid line) LHCII. C: second derivatives of the ^{15}N spectra in B.

Figure 3.4 shows an overlay of ^1H - ^{13}C HetCor spectra of quenched (red) and unquenched (blue) LHCII in the Arg $^{13}\text{C}_\zeta$ region (left panel) and $^{13}\text{C}_\delta$ region (right panel). The left panel presents the correlations between C_ζ and $\text{H}_{\eta_i}/\text{H}_\epsilon$, while the right panel presents the correlations between C_δ and H_δ (proton range 3-5 ppm) and between C_δ and H_ϵ (proton range 6-8.5 ppm). Since the H_ϵ proton signals (right panel) are in the range of 6.5-8.5 ppm, the proton responses in the left panel between 8.5-10.5 ppm are attributed to the H_{η_i} protons. The left panel also shows very peculiar well-resolved correlation signals

of narrow C_ζ responses at 156.8 ppm ^{13}C associated with very upfield shifted proton responses centered around 4.2 ppm ^1H .

Figure 3.5 shows the ^1H - ^{13}C HetCor spectra in the region of the Arg $^{13}\text{C}_\alpha$ responses (A, unquenched and B, quenched LHCII). The correlation signals in the range 62-64 ppm are attributed to ^{13}C natural abundance chemical shift signals of the detergent molecules. The Arg C_β and C_γ responses are strongly obscured by overlap with the detergent signals in the range 15-35 ppm and could not be resolved. A comparison of Fig. 3.5A and 3.5B shows that the C_α correlation peak signal at 57 ppm ^{13}C and 3.2 ppm ^1H in the spectrum of unquenched LHCII (Fig.3.5A) apparently shifts considerably downfield in the ^1H dimension and produces a doubled response for quenched LHCII (Fig.3.5B)

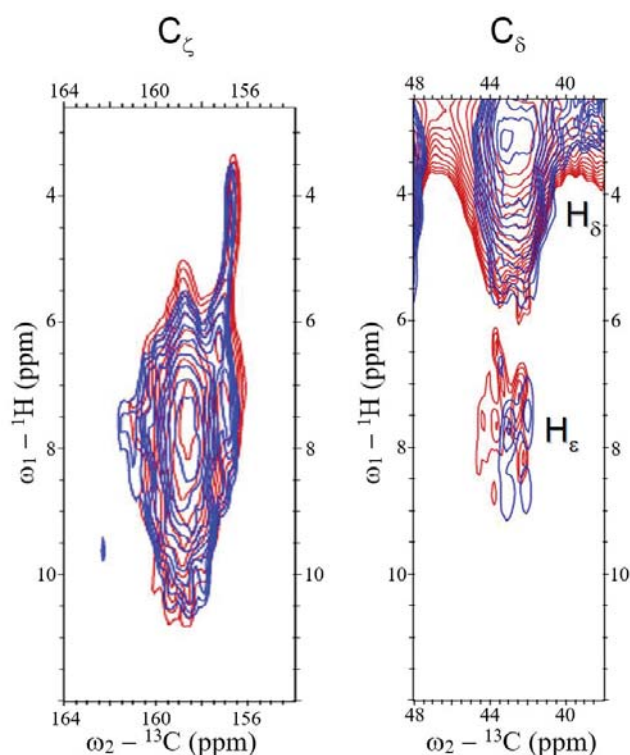


FIGURE 3.4. Heteronuclear ^1H - ^{13}C correlation spectra of unquenched (blue) and quenched (red) LHCII in the Arg $^{13}\text{C}_\zeta$ region (A) and in the $^{13}\text{C}_\delta$ region (B).

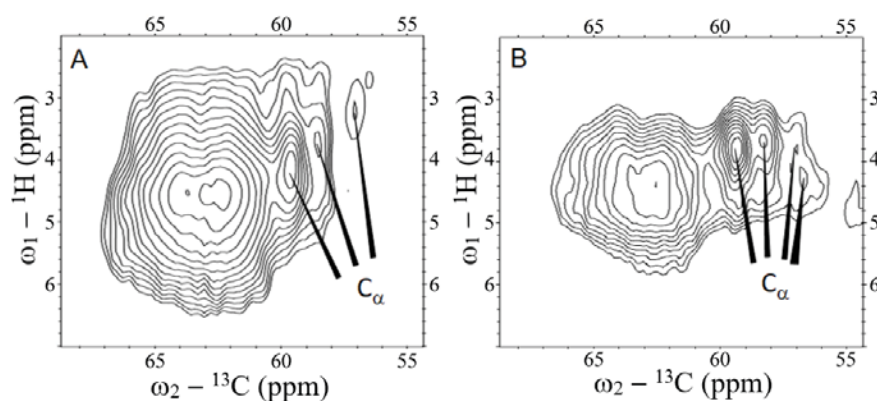


FIGURE 3.5. Heteronuclear ^1H - ^{13}C correlation spectra of unquenched (A) and quenched (B) LHCII in the Arg $^{13}\text{C}_\alpha$ region.

3.4. Discussion

The LHCII trimers *C. reinhardtii* are isomers composed of different Lhcbm polypeptides. These Lhcbm polypeptides contain 6 Arg residues that are conserved in the Lhcb sequences of *Arabidopsis thaliana*⁴⁰. The Lhcbm1, Lhcbm5 and Lhcbm10 polypeptides contain additional Arg residues (two for Lhcbm1 and 10 and one for Lhcbm5) very close to the N terminus, in a flexible part of LHCII that was not resolved in the LHCII X-ray structures. Most likely the NMR responses of these additional Arg are also unresolved in our NMR datasets, since they are only present in a subpopulation of the LHCII isomers. Moreover, their NMR responses are likely to be weakened due to intrinsic disorder of the N-terminal part, which causes dynamic broadening of the NMR lines and poor cross polarization. For example, in MAS NMR datasets of purple bacterial antenna proteins the terminal ends of the α and β polypeptides were not resolved⁵⁷.

Figure 3.6A shows the homology structure of the *C. reinhardtii* Lhcbm1 monomer, based on the *pea* LHCII X-ray structure (2BHW)³, with the 6 conserved Arg residues highlighted. Five Arg residues reside in the α -helical part of the protein while the sixth Arg is located in the stromal loop region. The arginines that form ion pairs with Glu and ligate Chls, R70, R185 and R160, are indicated in the figure, as well as R25 in the loop region. Figure 3.6B shows the arrangement of one of the stabilizing Arg-Glu pairs in detail: R70 and E180 that link helix A and B and ligate Chl610.

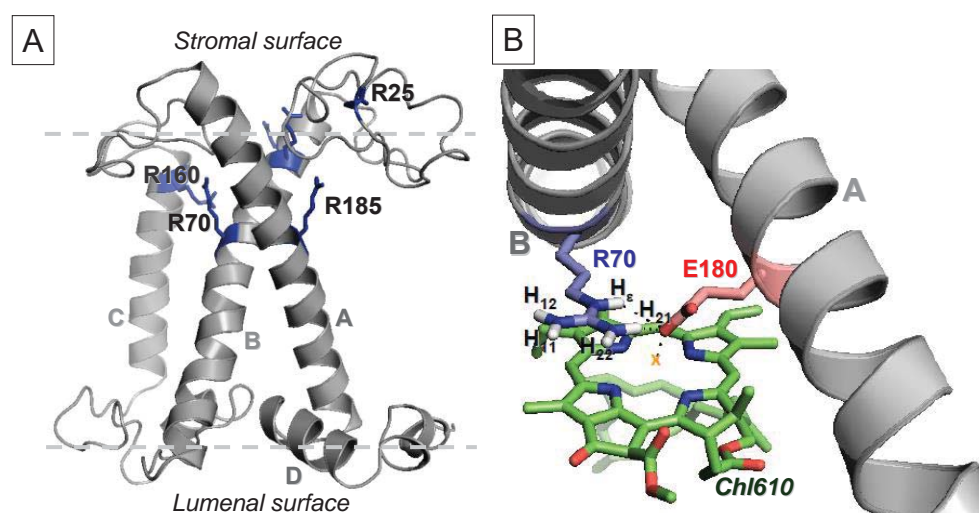


FIGURE 3.6.A: Homology structure of *C. reinhardtii* LHCII highlighting the Arg residues. B: The geometric arrangements of R70, E180 and Chl610 taken from the 2BHW (3) LHCII X-ray structure.

According to the plant LHCII X-ray structures, the 6 Arg residues are capable of forming hydrogen bonds via their side chain H_ε or H_η amides. The strong downfield NMR shifts of the Arg proton responses in the HetCor spectrum in Fig.3.4A suggest that also in *C. reinhardtii* LHCII strong hydrogen bonds are formed to the Arg residues that involve the NH_{ηi} amide protons.

3.4.1. Upfield shifted NMR responses are explained by Chl ringcurrent shifts for R70 and R185

In the HetCor spectrum in Figure 4, left panel, the ¹³C_ζ response at 156.8 ppm correlates with unusual upfield shifted proton responses at 4.2 ppm that are ~3 ppm shifted relative to the average values (7.4 and 6.8-6.9 ppm respectively) found for Arg H_ε and H_{ηi} in the Biological Magnetic Resonance Bank⁵⁸. To find an explanation for these unusual shifts, we estimated the ring current effects that are produced by the Chl macrocycle rings. Chl ring currents can induce large shifts for the NMR responses of atoms in close vicinity to the ring center-distances⁵⁹. Close inspection of the LHCII X-ray structures shows that both R70 and R185 have their side chains hanging over the macrocycle planes of the ligating Chls (Chl602 and 610) which positions the Arg side chain atoms close to the Chl rings. The third Arg residue involved in Chl ligation, R160, forms an ion pair with a Glu residue of the same helix (helix C) and has its side chain oriented perpendicular to the macrocycle plane of its ligating Chl (Chl609). For R160, only one proton is positioned close enough to the Chl ring center that it could experience significant ringcurrent effects.

The geometric arrangements of R70, E180 and Chl610 as shown in Fig.3.6B were taken from the 2BHW crystal structure and partially optimized as described in experimental procedure. Quantum-mechanical density-functional theory (DFT) calculations were performed for three structure models: (1) R70, (2) R70···E180 and (3) R70···E180···Chl610 to estimate the magnitude of Chl ringcurrent and H-bonding induced shifts of the R70 NMR responses. Table 3.1 shows how the chemical shifts of R70 (model 1) are affected by interaction with E180 (model 2) and by combined interaction with E180 and Chl610 (model 3). The effects of a partial geometry

optimization were most critical obvious for the calculated chemical shifts of the R70 H_ε and H₂₁ atoms. For these protons also non-optimized calculated shifts values are presented, in which the geometries were taken directly from the X-ray structure.

The results in Table 3.1 show that both for the unmodified and for the partially optimized structures the presence of the Chl causes strong ring current shifts for the R70 H_ε and H₂₁ responses of \sim -5 and \sim -3.5 ppm (i.e. the differences between the NMR responses calculated for model 2 and 3), which we attribute primarily to the ring currents in the Chl610 that counteract the large downfield shifts due to H-bonding of these protons to the E180 carboxyl. For H_ε, the H-bond interaction with the E180 carboxyl is weakened when a ligand to Mg is formed via the same oxygen atom, which may also affect the H_ε chemical shift.

The net effect of H-bonding and ring current shifts in our calculations are that the H_ε and H₂₁ NMR responses are shifted between +3.5 and -1 ppm, depending on the optimization procedure that was applied. The net effects for the other amide protons H₁₁, H₁₂ and H₂₂ are shifts between -1.5 and 2 ppm, while the side chain carbon responses of C_ζ and C_δ are shifted resp. -2.7 and -2.4 ppm.

Although the exact geometries of the Arg-Glu-Chl structures may differ in *C. reinhardtii* LHCII from the plant LHCII X-ray structures, the trends of the calculated chemical shift changes match with the experimental observations of i) C_ζ carbon responses that are shifted 2-3 ppm upfield from the bulk of C_ζ signals and that correlate with ii) proton responses that are shifted 0-2 ppm downfield in addition to iii) proton responses with significant upfield shifts, since for the H₁₁, H₁₂ and H₂₂ the interaction with E180 and Chl610 produces shifts of -1.5 to -2 ppm. Hence, according to the DFT chemical shift calculations, the upfield shifted ¹H-¹³C_ζ correlations that are well-resolved in Fig 3.4A could originate from Arg-Glu-Chl interactions involving the two Arg residues that form an important structural motif by locking helix A and B.

Our limited models do not take into account hydrogen bonds to other parts of the protein. In the LHCII X-ray structures, one amide proton of R70 is very close to the C13

TABLE 3.1. DFT-calculated NMR chemical shift effects on R70. The NMR chemical shifts of R70 were calculated using model (1): R70, model (2): R70···E180 and model (3): R70···E180···Chl610. Column 2: Chemical shift differences between model (2) and model (1). Column 3: Chemical shift differences between model (3) and model (1).

Atom	R70···E180 (model 2) $\Delta\sigma$ (ppm)	R70···E180···Chl610 (model 3) $\Delta\sigma$ (ppm)
H₈	+ 6.0 + 3.5*	+ 1.0 - 1.1*
H₁₁	- 1.1	- 1.5
H₁₂	- 0.9	- 1.7
H₂₁	+ 7.0 + 3.0*	+ 3.7 - 0.6*
H₂₂	- 0.8	- 2.1
C_ζ	- 1.2	- 2.7
C_δ	- 1.2	- 2.4
N_ζ	- 3.3	+ 1.3
N₁	+ 11.6	+ 9.5
N₂	- 8.1	- 6.8

keto carbonyl of Chl608. This proton is too far from the Chl ring centers to experience any ring current shift. A strong H-bond of this proton to the Chl608 carbonyl should induce a strong downfield shift of its NMR response. Instead, no strong downfield shifts are observed in the ¹H dimension for the C_ζ signal at 156.8 ppm. This suggests that the H-bonding patterns to the Chl side chains in *C. reinhardtii* LHCII differ from plant LHCII. In fact, in an earlier study on uniformly ¹³C-labeled *C. reinhardtii* LHCII we estimated that the number of Chls with H-bonded keto carbonyls is lower in *C. reinhardtii* LHCII

than in plant LHCII⁴⁰. Comparing the C_{ζ} regions in the HetCor spectra for quenched and unquenched LHCII (Fig.4), no significant changes are observed and the spectra are almost identical. In particular, the unusual correlation signal with very upfield proton shifts that we attribute to the helix-connecting Arg residues is preserved. The data imply that the Arg-Glu-Chl geometric arrangements are preserved in the quenched state, relative to the unquenched state. Since the Arg-Glu pairs interlock helix A and B, the conserved chemical-shift patterns suggest that the orientations of these two transmembrane helices, which define the tertiary structure, are also preserved in the two states. In addition, the Arg hydrogen bonding patterns appear to be preserved in the two forms of LHCII.

The DFT-calculated nitrogen chemical shifts of in Table 3.1 predict displacements of the Arg amide ^{15}N NMR responses when a hydrogen bond is formed to Glu (model 2), which breaks the symmetry of the $N_{\eta i}$ responses and induces an upfield shift of the N_{ε} response. The splitting of the Arg $^{15}\text{N}_{\eta}$ signal (Fig.3.3B and C) therefore can be explained by the induced asymmetry when a hydrogen bond is formed to one of the two N_{η} atoms, while splitting of the Arg N_{ε} signal is explained by heterogeneity of the Arg structures with respect to H-bonding of their side chain N_{ε} atoms.

3.4.2. In quenched LHCII, R25 changes its backbone conformation

The Arg $^{13}\text{C}_{\alpha}$ chemical shift responses reflect moderate conformational changes between the quenched and unquenched forms of LHCII. In the spectrum of unquenched LHCII two C_{α} correlation signals appear at 59.5 and 58.5 ppm and a smaller peak appears at 57 ppm. In the spectrum of quenched LHCII the latter peak is split into two weaker signals.

The LHCII X-ray structures 2BHW³ and 1RWT² were used to predict the Arg backbone chemical shifts using the SHIFTX2 server. The structure-predicted Arg C_{α} shifts range between 58-60 ppm for the residues in the α -helical stretches, while the Arg residue in the stromal loop region, R25, has a predicted C_{α} shift of 56 ppm. In the NMR spectrum of unquenched LHCII (Fig.5A), the relative signal intensities of the C_{α} peaks at 59.5, 58.5, and 57 ppm are roughly in the order of 3:2:1, matching with 5 Arg located in the α -helical stretches that have C_{α} shifts in the range 58-60 ppm and one Arg in the loop

region with a more upfield shifted C_α response. Therefore we tentatively assign the response at 57 ppm to the C_α of R25 in the stromal loop region. We cannot exclude that the response at 57 ppm $^{13}C_\alpha$ includes the additional Arg residues at the N-terminal site, appearing in a subpopulation of LHCII. The backbone NMR chemical shifts of the additional Arg residues will likely fall in the chemical-shift range for random-coil structures, *i.e.* 54-58 ppm.

Apparently, the backbone conformation of R25 (and/or of the additional Arg at the N-terminal ends) is changed in the photoprotective state (Fig.3.5B). R25 is in the water-exposed stromal region of the protein and this part of the protein is probably affected by a change in hydrophobicity or by protein-protein interactions inside the LHCII aggregates.

3.4.3. Stability of the interlocked A and B helices in the LHCII core: implications for possible conformational changes

Early studies of Murakami and Packer⁶⁰ showed a thinning of the thylakoid membrane bilayer upon illumination together with an increase in membrane hydrophobicity and similar effects were observed in electron microscopy micrographs of granal thylakoid membranes^{17,18}. Johnson et al. performed an extended analysis and demonstrated that apparent changes in the appressed membrane zone upon illumination correlated with structural changes in membrane thickness. The authors suggested that the observed decrease in membrane thickness reflects conformational changes of LHCII, forming a more ‘condensed’ state³⁵. A similar condensed state is proposed to form upon aggregation *in vitro* due to protein-protein interactions and changes in hydrophobicity²¹. Here we elaborate on this theory and reason that a hypothetical compressed conformation of LHCII can be established in two ways:

i) By increased helix tilting, which effect is a common response of membrane helices to hydrophobic mismatch^{61,62}. The LHCII monomers can be compressed by increasing the angles of the membrane-spanning helices A and B with respect to the membrane normal. This is illustrated in Figure 3.7B: the LHC structure in 3.7A is compressed by increased tilting of the interlocked helices, resulting in the structure drawn in 3.7B. However, such a mechanical movement would modify the geometric arrangements of the Glu and Arg residues linking the two helices, and of the Arg-Glu

ligated Chls (Fig.3.7B, encircled area). According to our results in Fig.3.4A this scenario is unlikely. The NMR data show that the responses of the involved Arg residues are almost identical for the quenched and unquenched forms of LHCII, while our modeling results predict that these responses are very sensitive to the specific orientations of the interacting Glu, Arg and Chls. Our findings match with the results of Dockter⁴² et al., which show that the LHCII polypeptides have low flexibility in the core region.

ii) Alternatively, a condensed state of LHCII can be created by rearrangement of protein segments located near the water interface. This is illustrated in Figure 3.7C, where segments at the stromal and luminal ends of the structure in Fig.3.7A are refolded (encircled areas) to create a more compact conformation. Such conformational changes are in line with the NMR data and can explain the variability of the $^{13}\text{C}_\alpha$ Arg response, which we tentatively attribute to rearrangement of R25 in the stromal region (Fig.3.5). While under our labeling conditions there are no residues reporting at the LHCII luminal site, it has been proposed that changes in luminal pH under NPQ conditions could enhance local refolding of the luminal loop region by protonation of acidic residues^{2,34}.

Photophysical quenching models have been proposed based on altered carotenoid-Chl interactions, in specific between lutein Lut620 and Chl*a*'s in the terminal-emitter domain (Chl610, 611 and 612)^{23,24}. According to our data results here on ^{13}C - ^{15}N -Arg LHCII, the ring current effects of Chl610 and 602 acting on R70 and R185 do not change in the quenched state. This is a strong indication that the orientations of Chl610 and of Chl602, which are in close distance with either of the two luteins in LHCII, are preserved. The position of Chl612 is also likely to be conserved, because its ligand N183 is close to the Arg-Glu interlocked helical core. Thus, photophysical quenching models based on altered lutein-Chl*a* interactions must involve a change in the orientation of a lutein chromophore with respect to the fixed positions of the adjacent Chls. Indeed, the quenched state of LHCII has been associated with a conformational change of the Lut620 carotenoid⁶³.

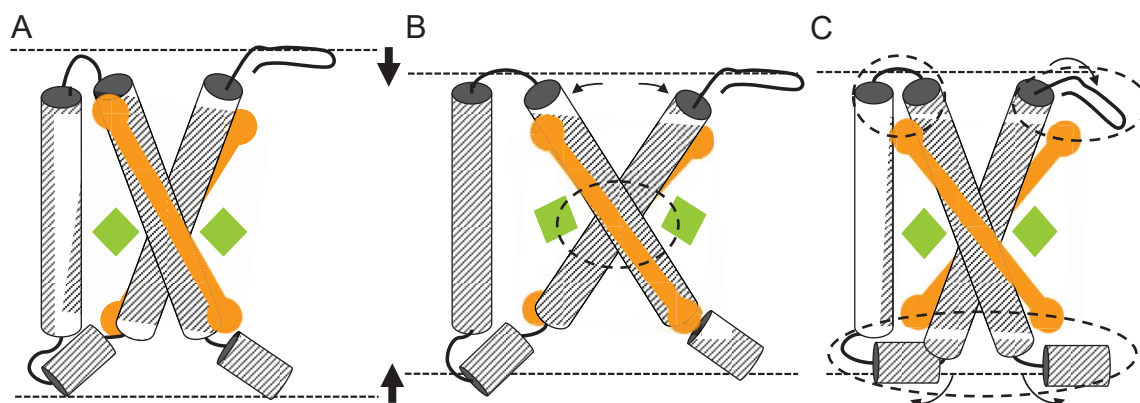


FIGURE 3.7. Cartoon picture illustrating the possible effects of membrane thinning on LHCII. Compression of the LHC structure in A is achieved by i) increased tilting of the transmembrane helices, causing structural changes in the Arg-Glu interlocked core (B; the affected core region is encircled) or ii) reorientation of protein segments close to the water in face, causing structural changes in the regions near the luminal and stromal sites (C; the affected end regions are encircled). A structural change as depicted in B will affect the orientations of Chl602 and 610 (green diamonds) that are ligated to the Arg-Glu interlocked core. However, such a structural rearrangement is unlikely according to the preserved NMR chemical shifts of the Chl-ligating Arg. The structural change depicted in C could reorient the the luteins (orange rods) that have their head groups bound to the affected protein end regions.

A change in the orientation of a lutein could affect the NMR responses of closely-spaced Chl carbons, explaining the quenching-related changes of specific LHCII Chl a NMR responses that were observed in⁴¹. Lut620 is stabilized by protein interactions via helix D and the loop segment connecting helix A and C. In a hypothetical, mechanistic model, changes in pH and hydrophobicity may re-orient these protein segments while maintaining the position of the interlocked helices A and B; resulting in a more compact protein structure as illustrated in Fig. 3.7C and moving Lut620 with respect to the fixed positions of Chl610 and 612, creating a photophysical quencher state.

3.5. Conclusion

We used a non-invasive method to selectively probe the structure and environment of the Arg residues in *C. reinhardtii* LHCII without the need for recombinant approaches. Our approach shows that solid-state NMR is a powerful method to determine the molecular structure of light-harvesting proteins while controlling their functional states.

Insights in the photoprotective switch of the Major LHC II

The conformations of the Arg residues in the α -helical regions near the stromal site and in the interlocked core are preserved in the light-harvesting and photoprotective states. In contrast, moderate changes are observed for the Arg in the stromal loop region. The results fit into a mechanistic picture where conformational changes of the LHCII end segments under NPQ conditions may re-orient a carotenoid with respect to the fixed positions of the Chls in the terminal emitting domain, rendering a photophysical response for dissipation of harmful excitation energies.

3.6. References

1. Ballottari, M., Girardon, J., Dall'Osto, L. & Bassi, R. Evolution and functional properties of Photosystem II light harvesting complexes in eukaryotes. *Biochim. Biophys. Acta - Bioenerg.* **1817**, 143–157 (2012).
2. Liu, Z. *et al.* Crystal structure of spinach major light-harvesting complex at 2.72 Å resolution. *Nature* **428**, 287–292 (2004).
3. Standfuss, J., Terwisscha van Scheltinga, A. C., Lamborghini, M. & Kühlbrandt, W. Mechanisms of photoprotection and nonphotochemical quenching in pea light-harvesting complex at 2.5 Å resolution. *EMBO J.* **24**, 919–28 (2005).
4. Barros, T. & Kühlbrandt, W. Crystallisation, structure and function of plant light-harvesting Complex II. *Biochim. Biophys. Acta* **1787**, 753–72 (2009).
5. Ruban, A. V, Johnson, M. P. & Duffy, C. D. P. The photoprotective molecular switch in the photosystem II antenna. *Biochim. Biophys. Acta - Bioenerg.* **1817**, 167–181 (2012).
6. Horton, P. Optimization of light harvesting and photoprotection: molecular mechanisms and physiological consequences. *Philos. Trans. R. Soc. B Biol. Sci.* **367**, 3455–3465 (2012).
7. Szabó, I., Bergantino, E. & Giacometti, G. M. Light and oxygenic photosynthesis: energy dissipation as a protection mechanism against photo-oxidation. *EMBO Rep.* **6**, 629–634 (2005).
8. Li, X.-P. *et al.* A pigment-binding protein essential for regulation of photosynthetic light harvesting. *Nature* **403**, 391–395 (2000).
9. Li, X.-P. *et al.* Regulation of Photosynthetic Light Harvesting Involves Intrathylakoid Lumen pH Sensing by the PsbS Protein. *J. Biol. Chem.* **279**, 22866–22874 (2004).
10. Walters, R. G., Ruban, A. V. & Horton, P. Identification of proton-active residues in a higher plant light-harvesting complex. *Proc. Natl. Acad. Sci.* **93**, 14204 LP – 14209 (1996).
11. Müller, P., Li, X.-P. & Niyogi, K. K. Non-Photochemical Quenching. A Response to Excess Light Energy. *Plant Physiol.* **125**, 1558 LP – 1566 (2001).
12. Bonente, G. *et al.* Analysis of LhcSR3, a Protein Essential for Feedback De-Excitation

- in the Green Alga *Chlamydomonas reinhardtii*. *PLOS Biol.* **9**, e1000577 (2011).
13. Bonente, G. *et al.* The Occurrence of the psbS Gene Product in *Chlamydomonas reinhardtii* and in Other Photosynthetic Organisms and Its Correlation with Energy Quenching†. *Photochem. Photobiol.* **84**, 1359–1370 (2008).
 14. Peers, G. *et al.* An ancient light-harvesting protein is critical for the regulation of algal photosynthesis. *Nature* **462**, 518–521 (2009).
 15. Ferrante, P., Ballottari, M., Bonente, G., Giuliano, G. & Bassi, R. LHCBM1 and LHCBM2/7 Polypeptides, Components of Major LHCII Complex, Have Distinct Functional Roles in Photosynthetic Antenna System of *Chlamydomonas reinhardtii*. *J. Biol. Chem.* **287**, 16276–16288 (2012).
 16. Elrad, D., Niyogi, K. K. & Grossman, A. R. A Major Light-Harvesting Polypeptide of Photosystem II Functions in Thermal Dissipation. *Plant Cell* **14**, 1801 LP – 1816 (2002).
 17. Johnson, M. P. *et al.* Photoprotective Energy Dissipation Involves the Reorganization of Photosystem II Light-Harvesting Complexes in the Grana Membranes of Spinach Chloroplasts. *Plant Cell* **23**, 1468 LP – 1479 (2011).
 18. Kirchhoff, H. *et al.* Dynamic control of protein diffusion within the granal thylakoid lumen. *Proc. Natl. Acad. Sci.* **108**, 20248 LP – 20253 (2011).
 19. Goral, T. K. *et al.* Visualising the mobility and distribution of chlorophyll-proteins in higher plant thylakoid membranes: effects of photoinhibition and protein phosphorylation. *Plant J.* **0**, (2010).
 20. Betterle, N. *et al.* Light-induced Dissociation of an Antenna Hetero-oligomer Is Needed for Non-photochemical Quenching Induction. *J. Biol. Chem.* **284**, 15255–15266 (2009).
 21. Ruban, A. V, Johnson, M. P. & Duffy, C. D. P. The photoprotective molecular switch in the photosystem II antenna. *Biochim. Biophys. Acta* **1817**, 167–81 (2012).
 22. Barros, T., Royant, A., Standfuss, J., Dreuw, A. & Kühlbrandt, W. Crystal structure of plant light-harvesting complex shows the active, energy-transmitting state. *EMBO J.* **28**, 298–306 (2009).
 23. Bode, S. *et al.* On the regulation of photosynthesis by excitonic interactions between carotenoids and chlorophylls. *Proc. Natl. Acad. Sci.* **106**, 12311 LP – 12316 (2009).

Chapter 3

24. Ruban, A. V *et al.* Identification of a mechanism of photoprotective energy dissipation in higher plants. *Nature* **450**, 575–578 (2007).
25. Miloslavina, Y. *et al.* Far-red fluorescence: A direct spectroscopic marker for LHCII oligomer formation in non-photochemical quenching. *FEBS Lett.* **582**, 3625–3631 (2008).
26. Liao, P.-N. *et al.* On the role of excitonic interactions in carotenoid–phthalocyanine dyads and implications for photosynthetic regulation. *Photosynth. Res.* **111**, 237–243 (2012).
27. Berera, R. *et al.* A simple artificial light-harvesting dyad as a model for excess energy dissipation in oxygenic photosynthesis. *Proc. Natl. Acad. Sci.* **103**, 5343 LP – 5348 (2006).
28. Holt, N. E. *et al.* Carotenoid Cation Formation and the Regulation of Photosynthetic Light Harvesting. *Science (80-.)*. **307**, 433 LP – 436 (2005).
29. Krüger, T. P. J., Novoderezhkin, V. I., Iliaia, C. & van Grondelle, R. Fluorescence Spectral Dynamics of Single LHCII Trimers. *Biophys. J.* **98**, 3093–3101 (2010).
30. Ruban, A. V & Horton, P. Mechanism of Δ pH-dependent dissipation of absorbed excitation energy by photosynthetic membranes. I. Spectroscopic analysis of isolated light-harvesting complexes. *Biochim. Biophys. Acta - Bioenerg.* **1102**, 30–38 (1992).
31. Pascal, A. A. *et al.* Molecular basis of photoprotection and control of photosynthetic light-harvesting. *Nature* **436**, 134–137 (2005).
32. van Oort, B. *et al.* Different crystal morphologies lead to slightly different conformations of light-harvesting complex II as monitored by variations of the intrinsic fluorescence lifetime. *Phys. Chem. Chem. Phys.* **13**, 12614–12622 (2011).
33. Pandit, A. *et al.* Assembly of the Major Light-Harvesting Complex II in Lipid Nanodiscs. *Biophys. J.* **101**, 2507–2515 (2011).
34. Yang, C. *et al.* The negatively charged amino acids in the luminal loop influence the pigment binding and conformation of the major light-harvesting chlorophyll a/b complex of photosystem II. *Biochim. Biophys. Acta - Bioenerg.* **1777**, 1463–1470 (2008).
35. Johnson, M. P., Brain, A. P. R. & Ruban, A. V. Changes in thylakoid membrane thickness associated with the reorganization of photosystem II light harvesting

- complexes during photoprotective energy dissipation. *Plant Signal. Behav.* **6**, 1386–1390 (2011).
36. Pandit, A. & de Groot, H. J. M. Solid-state NMR applied to photosynthetic light-harvesting complexes. *Photosynth. Res.* **111**, 219–226 (2012).
37. Pandit, A., Buda, F., van Gammeren, A. J., Ganapathy, S. & de Groot, H. J. M. Selective Chemical Shift Assignment of Bacteriochlorophyll a in Uniformly [13C–15N]-Labeled Light-Harvesting 1 Complexes by Solid-State NMR in Ultrahigh Magnetic Field. *J. Phys. Chem. B* **114**, 6207–6215 (2010).
38. Pandit, A. *et al.* Nuclear Magnetic Resonance Secondary Shifts of a Light-Harvesting 2 Complex Reveal Local Backbone Perturbations Induced by Its Higher-Order Interactions. *Biochemistry* **49**, 478–486 (2010).
39. van Gammeren, A. J. *et al.* Selective Chemical Shift Assignment of B800 and B850 Bacteriochlorophylls in Uniformly [13C,15N]-Labeled Light-Harvesting Complexes by Solid-State NMR Spectroscopy at Ultra-High Magnetic Field. *J. Am. Chem. Soc.* **127**, 3213–3219 (2005).
40. Pandit, A. *et al.* First solid-state NMR analysis of uniformly 13C-enriched major light-harvesting complexes from *Chlamydomonas reinhardtii* and identification of protein and cofactor spin clusters. *Biochim. Biophys. Acta - Bioenerg.* **1807**, 437–443 (2011).
41. Pandit, A. *et al.* An NMR comparison of the light-harvesting complex II (LHCII) in active and photoprotective states reveals subtle changes in the chlorophyll a ground-state electronic structures. *Biochim. Biophys. Acta - Bioenerg.* **1827**, 738–744 (2013).
42. Dockter, C. *et al.* Rigid Core and Flexible Terminus: Structure of solubilized light-harvesting Chlorophyll a/b complex (LHCII) measured by EPR. *J. Biol. Chem.* **287**, 2915–2925 (2012).
43. Gorman, D. S. & Levine, R. P. Cytochrome f and plastocyanin: their sequence in the photosynthetic electron transport chain of *Chlamydomonas reinhardtii*. *Proc. Natl. Acad. Sci.* **54**, 1665 LP – 1669 (1965).
44. Naumann, B., Stauber, E. J., Busch, A., Sommer, F. & Hippler, M. N-terminal Processing of Lhca3 Is a Key Step in Remodeling of the Photosystem I-Light-harvesting Complex Under Iron Deficiency in *Chlamydomonas reinhardtii*. *J. Biol. Chem.* **280**, 20431–20441 (2005).

Chapter 3

45. Drop, B. *et al.* Photosystem I of *Chlamydomonas reinhardtii* Contains Nine Light-harvesting Complexes (Lhca) Located on One Side of the Core. *J. Biol. Chem.* **286**, 44878–44887 (2011).
46. Germano, M. *et al.* Supramolecular organization of photosystem I and light-harvesting complex I in *Chlamydomonas reinhardtii*. *FEBS Lett.* **525**, 121–125 (2002).
47. Joris Snellenburg, Sergey Laptinok, Ralf Seger, Katharine Mullen, I. van S. Glotaran: A Java-based graphical user interface for the R package TIMP. *J. Stat. Softw.* **49**, hal-00817159 (2012).
48. Wawrzyniak, P. K. *et al.* Protein-induced geometric constraints and charge transfer in bacteriochlorophyll–histidine complexes in LH2. *Phys. Chem. Chem. Phys.* **10**, 6971–6978 (2008).
49. Becke, A. D. Density-functional exchange-energy approximation with correct asymptotic behavior. *Phys. Rev. A* **38**, 3098–3100 (1988).
50. Miehlich, B., Savin, A., Stoll, H. & Preuss, H. Results obtained with the correlation energy density functionals of Becke and Lee, Yang and Parr. *Chem. Phys. Lett.* **157**, 200–206 (1989).
51. Lee, C., Yang, W. & Parr, R. G. Development of the Colle-Salvetti correlation-energy formula into a functional of the electron density. *Phys. Rev. B* **37**, 785–789 (1988).
52. Facelli, J. C. Density Functional Theory Calculations of the Structure and the ¹⁵N and ¹³C Chemical Shifts of Methyl Bacteriopheophorbide a and Bacteriochlorophyll a. *J. Phys. Chem. B* **102**, 2111–2116 (1998).
53. Ditchfield, R. Theoretical studies of the temperature dependence of magnetic shielding tensors: H₂, HF, and LiH. *Chem. Phys.* **63**, 185–202 (1981).
54. Wolinski, K., Hinton, J. F. & Pulay, P. Efficient implementation of the gauge-independent atomic orbital method for NMR chemical shift calculations. *J. Am. Chem. Soc.* **112**, 8251–8260 (1990).
55. McWeeny, R. Perturbation Theory for the Fock-Dirac Density Matrix. *Phys. Rev.* **126**, 1028–1034 (1962).
56. Woliński, K. & Sadlej, A. J. Self-consistent perturbation theory. *Mol. Phys.* **41**, 1419–1430 (1980).

57. Gammeren, A. J. van, Hulsbergen, F. B., Hollander, J. G. & Groot, H. J. M. de. Residual backbone and side-chain ^{13}C and ^{15}N resonance assignments of the intrinsic transmembrane light-harvesting 2 protein complex by solid-state Magic Angle Spinning NMR spectroscopy. *J. Biomol. NMR* **31**, 279–293 (2005).
58. Ulrich, E. L. *et al.* BioMagResBank. *Nucleic Acids Res.* **36**, D402–D408 (2008).
59. Abraham, R. J. & Smith, K. M. NMR spectra of porphyrins. 21. Applications of the ring-current model to porphyrin and chlorophyll aggregation. *J. Am. Chem. Soc.* **105**, 5734–5741 (1983).
60. Murakami, S. & Packer, L. Protonation and Chloroplast membrane structure. *J. Cell Biol.* **47**, 332 LP – 351 (1970).
61. Park, S. H. & Opella, S. J. Tilt Angle of a Trans-membrane Helix is Determined by Hydrophobic Mismatch. *J. Mol. Biol.* **350**, 310–318 (2005).
62. Kim, T. & Im, W. Revisiting Hydrophobic Mismatch with Free Energy Simulation Studies of Transmembrane Helix Tilt and Rotation. *Biophys. J.* **99**, 175–183 (2010).
63. Iliaia, C. *et al.* Photoprotection in Plants Involves a Change in Lutein 1 Binding Domain in the Major Light-harvesting Complex of Photosystem II. *J. Biol. Chem.* **286**, 27247–27254 (2011).

Chapter 3

Structure determination of self-aggregated and semi synthetically prepared Zn 3¹-amino chlorin with MAS NMR and molecular modelling.

Magic Angle Spinning NMR has been used to investigate the self-assembled structure of a semi-synthetic self-aggregated artificial light harvesting antenna system. The self-assembly of a Zn 3¹-amino chlorin compound containing ¹³C at natural abundance was studied by ¹H-¹³C heteronuclear Magic-Angle Spinning (HETCOR MAS) NMR spectroscopy. Zn 3¹-amino chlorin was derived from naturally occurring chlorophyll *a*. The molecule was prepared by removing the side chain methyl group at the 3¹-amine position of a Zn 3¹-methylamino chlorin compound. From ¹H-¹³C HETCOR MAS NMR experiments, ¹H and ¹³C chemical shifts assignments for Zn 3¹-amino chlorin were obtained and the corresponding aggregation shifts relative to the monomer shifts in solution were determined. Large ¹H aggregation shifts up to 11.4 ppm were observed, which reveal a closely packed stacking of molecules with overlapping macrocycles in the aggregate structure. Strong aggregation shifts of the 12¹, 3¹ and 2¹ protons provide evidence for a *syn-anti* parallel stack model in which the vertical stacks are laterally associated. We conclude that the removal of the 3¹-methyl group leads to tight packing of the molecules, with strong lateral hydrogen bonds formed between the side chain NH and CO groups of the adjacent molecules.

4.1. Introduction

In Nature, chlorosomes in sulfur bacteria act as highly efficient light energy transfer systems and make it possible to survive under extreme low light conditions with single chlorophyll photon absorption rates of less than-one photon per hour¹⁻⁶. The highly ordered, self-organized chlorosome structures have the capacity of harvesting light and transfer of the excitation energy over long distances through pigment-pigment interactions, *i.e.* by collective dielectric properties *via* alignment of their electric transition dipoles, hydrogen bond interactions and molecular overlap⁷⁻¹³. Semisynthetic artificial light-harvesting antenna molecules can mimic these properties and such self-assemblies can act as highly conductive nanowires¹⁴⁻¹⁷. Effective methodologies are required to reveal the packing order inside the antenna complexes for rational and directed design of novel materials for artificial light harvesting and catalytic energy conversion. The lack of long-range order in chlorosomes and their variability in size make high-resolution diffraction methods unsuitable to determine the molecular stacking pattern.

The intriguing self-aggregation capacity of bacteriochlorophyll *c* (BChl *c*) in chlorosomes has been mimicked by using a semi-synthetic approach, in which the dye molecules are preprogrammed for self-aggregation. Tamiaki *et al* developed Zn 3¹-hydroxy chlorin semi-synthetically, for which the spectral properties are similar to naturally occurring Bchls¹⁸. 3¹-hydroxyalkyl and 3¹-methoxyalkyl Zn-chlorins were semi-synthetically prepared from naturally occurring Chl *a* by Huber *et al*, and their self-assembled structures were determined by Ganapathy *et al* by combining solid state NMR and X-ray diffraction together with molecular modeling and quantum mechanical (QM) calculations¹⁹⁻²¹. Pandit *et al* demonstrated that the self-assembled structure of a Zn 3¹-aminomethyl chlorin could be determined solely using solid-state NMR as a spectroscopic technique, by comparing the NMR structure with a library of possible stacking modes²². Self-assemblies of the Zn 3¹-hydroxyalkyl chlorin and Zn 3¹-methoxyalkyl chlorin showed symmetric NMR ring current shifts of the 2¹ and 12¹ protons, due to lateral packing interactions between vertical anti-parallel stacks. It was anticipated that these lateral interactions should be stabilized in stacks of the Zn 3¹-aminomethyl chlorin since

the amino group allows the formation of lateral hydrogen bonds between the NH and CO groups of adjacent chlorins. However, self-assemblies of this compound showed large ring current shifts for the 3¹ and 3³ protons and only very moderate shifts for the 2¹ and 12¹ protons were observed. Molecular stacking models of the Zn 3¹-aminomethyl chlorin suggested that the 3³ methyl group prevents lateral hydrogen bonding of the amino group by steric hindrance.

In this study, we analyzed the structure of a Zn 3¹-amino chlorin (ZnChl) shown in Figure 4.1, in which the 3³-methyl is absent. We show that the stacking of this ZnChl compound into self-aggregates induces large ring current shifts on both sides of the molecule, for the 3¹ as well as for the 2¹ and 12¹ protons. From this result, we propose that removal of the 3³ methyl group enables the formation of *syn-anti* parallel stacks with strong lateral interactions among the stacks, in contrast to the antiparallel stacking determined previously for the 3¹-hydroxyalkyl and 3¹-methoxyalkyl Zn-chlorins²¹.

4.2. Materials and Methods

4.2.1. Preparation of ZnChl aggregates

Aggregates were prepared by adding 100 times excess of n-hexane to the ZnChl dissolved in CH₂Cl₂ or THF^{16,23,24}. The sample was incubated at 4°C in the dark to form precipitates. The solvents were dehydrated using an aluminum column and stored over 4 Å molecular sieves. The pellet was transferred to a 4 mm CRAMPS rotor and dried under vacuum overnight. All the steps were performed under dim green light and nitrogen flow to prevent photodamage.

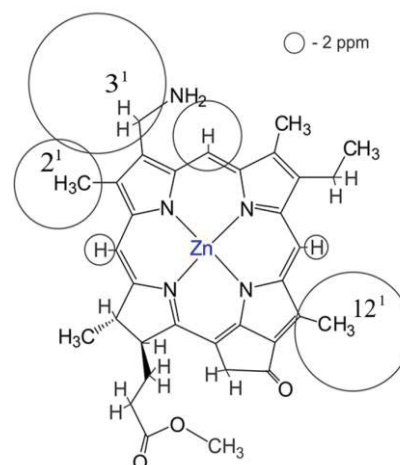


Figure 4.1. The aggregation shifts of ZnChl relative to their monomer in THF-*d*₆ are indicated with circle and the size of the circle is proportional to the observed aggregation shifts.

4.2.2. Solid state NMR experiments

MAS NMR experiments were performed at a sample temperature of 293K with a Bruker-750 spectrometer equipped with a 4-mm triple resonance MAS probe head using a ^{13}C radiofrequency of 188.6 MHz and a spinning frequency of 13 kHz. The ^1H chemical shift scale was calibrated from a Frequency Switched Lee-Goldburg (FSLG) heteronuclear correlation (HETCOR) spectrum of solid tyrosine HCl salt²⁵. 2D ^1H - ^{13}C hetero nuclear correlation data sets of the ZnChl aggregates were obtained using a cross polarization time of 0.25 ms. Monomers of the ZnChl were prepared by dissolving the compound in THF- d_8 and were analyzed by solution NMR. The ^1H and ^{13}C chemical shifts of the monomer were determined from 1D ^1H , ^{13}C APT, 2D ^1H - ^1H COSY and ^1H - ^{13}C HSQC NMR spectra recorded on a DMX-600 spectrometer.

4.2.3. Molecular modeling

The molecules were drawn and initial geometry optimizations were performed. The charges obtained from DMol³ calculation which uses density functional theory, were used for initial optimization. Chemical shift calculations were performed for slabs of ZnChl stacks with the CASTEP code, which utilizes the gauge-including projector augmented wave algorithm (GIPAW). Calculations utilized the generalized gradient approximation (GGA), revised Perdew, Burke and Ernzerhof (rPBE) functional with on-the-fly pseudopotentials, a k-point spacing of 0.08 Å, and a plane wave basis set cut-off energy of 500 eV. Unit cell parameter optimization of the proposed unit cell under periodic boundary conditions was done with the LDA CA-PZ functional²⁶⁻³¹.

4.3. RESULTS AND DISCUSSION

4.3.1. Absorption spectra of monomer and aggregates of ZnChl

Aggregation of the ZnChl compound was confirmed by a red shift of the Q_Y absorption maximum, *i.e.* a decrease of the monomer Q_Y band at 645 nm and an absorption increase for the aggregation band at 725 nm (Figure 4.2.)²⁰.

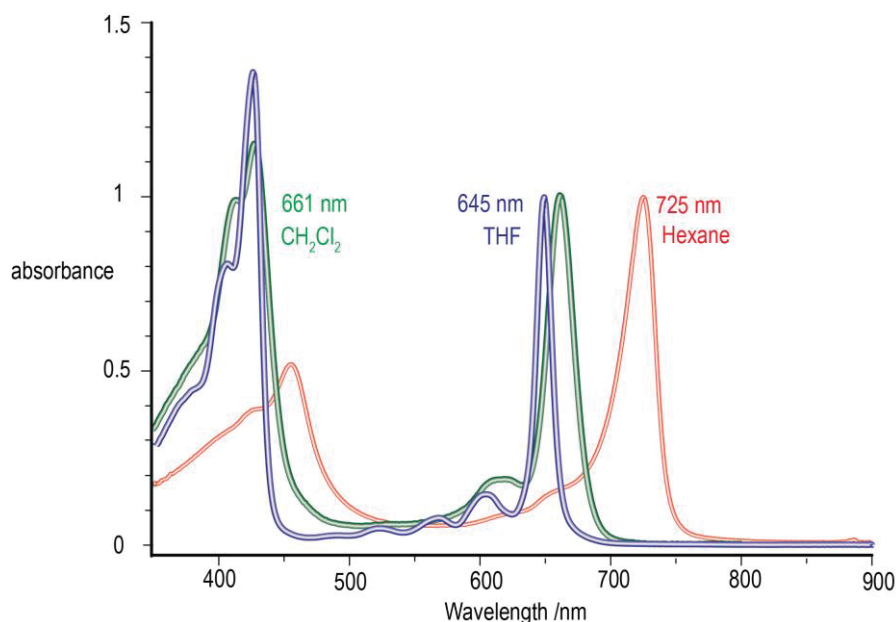


Figure 4.2. Absorption spectra of ZnChl in THF (monomers) and THF/n-hexane (8:100, aggregate form).

4.3.2. NMR responses for monomer and aggregates of ZnChl

Figure 4.3. shows the 1D ¹³C CP-MAS spectrum of the ZnChl aggregates. Narrow resonances in the spectrum indicate a well-ordered arrangement of the molecules in the packing. Figure 4.4. shows the 2D HETCOR ¹H-¹³C spectrum at a cross polarization contact time of 0.256 ms in which the proton assignments are indicated. The solid-state proton shift values are listed in Table 4.1 as $\sigma^{\text{H}}_{\text{solid}}$. The aggregation shifts are calculated as the chemical shifts in the solid-state relative to the chemical shifts for the monomer in solution. The ¹H monomer shifts for the ZnChl $\sigma^{\text{H}}_{\text{liq}}$ and the aggregation shifts $\Delta\sigma^{\text{H}}_i = \sigma^{\text{H}}_{\text{liq}} - \sigma^{\text{H}}_{\text{solid}}$ are listed in Table 4.1. Significant upfield chemical shifts are observed and are depicted as circles for aggregation shift values, which are obtained by less than -2 ppm in Figure 4.1, where the circle radius is proportional to the magnitude of the shift. These aggregation shifts are dominated by ring current effects that are also observed in another semi synthetically prepared Zn and Cd chlorins^{32,33}. The cross-correlation peaks for C5, C10 and C20 show splitting of signals in both the ¹H and ¹³C dimensions in Figure 4.4, indicative of two slightly different conformers of ZnChl molecules in the stacks. A second peak is observed at the same resonance position in the ¹³C dimension for 3¹ in the ¹H-¹³C

Chapter 4

HETCOR spectrum (Figure 4.4.). We tentatively attribute this peak to the side chain NH proton. Protons with significant ^1H upfield shifts are indicated in the correlation plot shown in Figure 4.5.

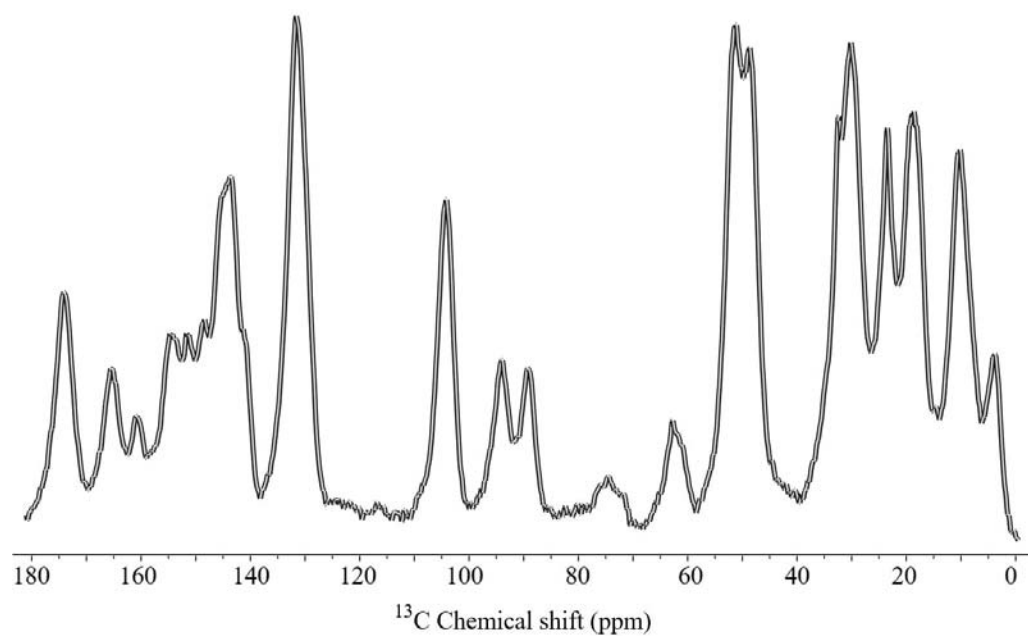


Figure 4.3. ^{13}C CP-MAS spectrum of ZnChl aggregates.

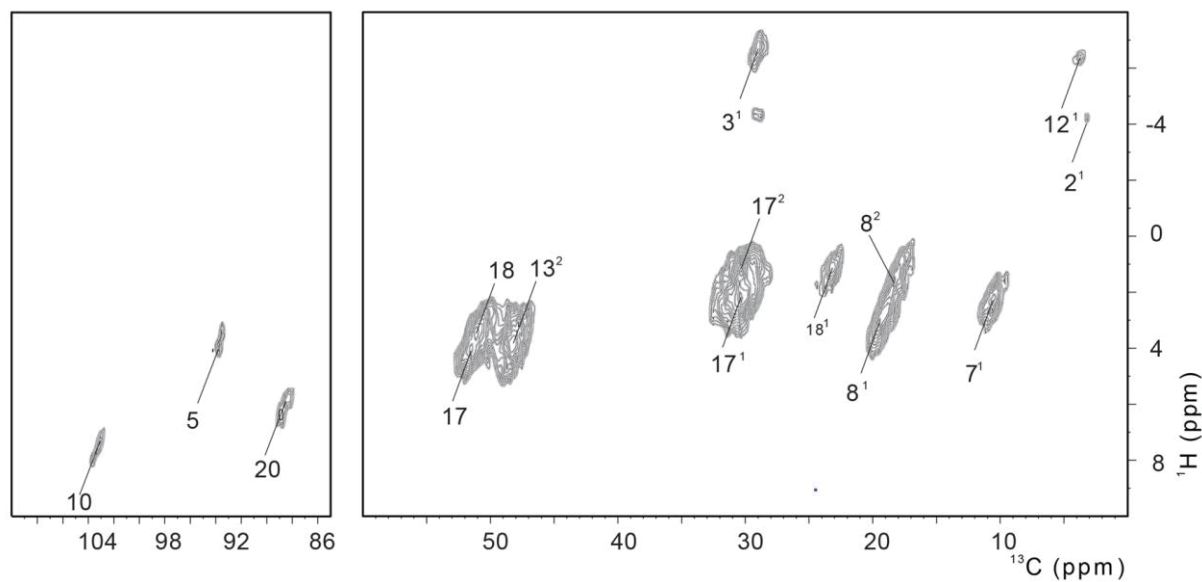


Figure 4.4. ^1H - ^{13}C HETCOR spectrum of ZnChl aggregates collected at a cross polarization contact time of 0.256 ms.

Structural determination of self-aggregated Zn 3¹-amino chlorin

Table 4.1. ¹H chemical shifts for ZnChl in solution ($\sigma^{\text{H}}_{\text{liq}}$) and in aggregates ($\sigma^{\text{H}}_{\text{solid}}$) and the aggregation shifts $\Delta \sigma^{\text{H}}_i$.

Position	$\sigma^{\text{H}}_{\text{liq}}$	$\sigma^{\text{H}}_{\text{solid}}$	$\Delta \sigma^{\text{H}}_i = \sigma^{\text{H}}_{\text{liq}} - \sigma^{\text{H}}_{\text{solid}}$
2 ¹	3.29	-4.21	-7.5
3 ¹	5.04	-6.72	-11.76
5	9.57	3.7	-5.87
7 ¹	3.29	2.21	-1.08
8 ¹	3.8	2.92	-0.88
8 ²	1.71	1.55	-0.16
10	9.61	7.6	-2
12 ¹	3.61	-6.37	-9.98
13 ²	5.04	3.91	-1.13
17	4.31	4.17	-0.14
17 ¹	2.6	2.1	-0.5
17 ²	2.3	1.16	-1.14
17 ⁴	3.54	4.00	0.46
18	4.52	3.4	-1.12
18 ¹	1.79	1.14	-0.65
20	8.48	5.9	-2.58

The observable NH resonance for ZnChl here indicates a relatively rigid 3¹ side chain in the stacks, in agreement with hydrogen bonding of the side chain amino protons. In comparison with the 3¹-hydroxy Zn chlorins studied by Ganapathy *et al.*²¹ there is a similar pattern for the C5, C10, C20, C3¹ and C12¹ chemical shifts. However, larger ring current shifts are observed for the ZnChl compound, *i.e.* -11.4 ppm for the 3¹-methyl, -7.5 ppm for 2¹-methyl and -9.9 ppm for 12¹-methyl protons. The chemical shift for the C7¹, C8¹ and C8² are similar to the previously studied Zn 3¹-aminomethyl chlorin from Pandit *et al.*²². In contrast to the Zn 3¹-aminomethyl chlorin studied by Pandit *et al.*, but similar to the Zn 3¹-hydroxyalkyl chlorin and Zn 3¹-methoxyalkyl chlorin, ZnChl shows significant ring current shifts for the 12¹ and 2¹ protons²². It was assumed that the strong lateral interactions present in aggregates of Zn 3¹-hydroxyalkyl chlorin and Zn 3¹-methoxyalkyl chlorin are lacking in the Zn 3¹-aminomethyl chlorin because of steric hindrance induced by the 3³-methyl group. In our present compound, we propose that the lack of 3³-methyl

Chapter 4

group apparently makes it possible to form lateral associates via intermolecular hydrogen bonds (NH•••CO).

Table 4.2. ^{13}C chemical shifts for ZnChl in solution ($\sigma^{C_{liq}}$) and in aggregates ($\sigma^{C_{solid}}$) and the aggregation shifts $\Delta\sigma^{C_i}$.

Position	$\sigma^{C_{liq}}$ (ppm)	$\sigma^{C_{solid}}$ (ppm)	$\Delta\sigma^{C_i} = \sigma^{C_{liq}} - \sigma^{C_{solid}}$
13 ¹	195.48	192.87	-2.61
17 ³	173.80	174.02	0.22
19	168.86	165.49	-3.37
14	161.83	160.61	-1.22
16	156.96	154.09	-2.87
1	154.85	154.09	-0.76
6	151.79	151.23	-0.56
4	149.33	148.67	-0.66
11	148.30	148.67	0.37
9	145.99	145.32	-0.67
8	144.11	144.85	0.74
3	141.06	140.88	-0.18
2	137.11	131.63	-5.48
7	133.91	131.63	-2.28
12	133.73	131.63	-2.10
13	133.19	131.63	-1.56
10	106.34	104.70	-1.64
15	106.43	104.70	-1.73
5	99.62	93.91	-5.71
20	92.57	88.83	-3.74
3 ¹	40.99	29.05	-11.94
17	51.58	51.39	-0.19
18	49.80	48.46	-1.34
17 ⁴	51.00	51.39	0.39
13 ²	48.90	48.46	-0.44
17 ²	31.02	30.41	-0.61
17 ¹	30.75	29.35	-1.40
18 ¹	23.94	23.36	-0.58
8 ¹	20.29	18.54	-1.75
8 ²	18.10	18.16	0.06
7 ¹	11.44	10.42	-1.02
2 ¹	11.23	10.42	-0.81
12 ¹	12.59	3.78	-8.81

Except for the long tail and methoxy or hydroxy side group, the chemical structure of ZnChl is identical to the compounds in Zn 3¹-hydroxyalkyl chlorin, Zn 3¹-methoxyalkyl chlorin and a similar pattern of ring current shifts for the 3¹, 2¹, 12¹ protons occurs. Hence, the stacking mode for our compound will likely be similar, *i.e.* consist of aggregates that are formed by laterally associated a syn-anti parallel stacks. The narrow lines of the 1D CP-MAS spectrum of the aggregate (Figure 4.3) suggest that it forms a microcrystalline material. Similar narrow lines are observed for self-assemblies of Cd and other types of Zn chlorins^{19,22}.

The observed ring current shift pattern of the 12¹ and 2¹ protons would in principal agree with a parallel mode of stacking, however in parallel mode each chlorin experiences the ring current shift from one neighbor chlorin only and therefore the magnitudes of the ring current shifts are moderate. In contrast, in the stack model of Zn 3¹-

hydroxyalkyl chlorin and Zn 3¹-methoxyalkyl chlorin by Ganapathy *et al*, which are very similar to ZnChl, each chlorin experiences ring current effects from two lateral neighbors, so the observed ring current shifts are large²¹. Thus, the magnitude of the 12¹ and 2¹ aggregation shifts suggest that the ZnChl is likely to assemble in similar fashion as the Zn 3¹-hydroxyalkyl chlorin and Zn 3¹-methoxyalkyl chlorin.

We observed here the largest aggregation shifts for a Zn chlorin reported so far for the members of Zn chlorin family. The aggregation shifts for the 12¹ and 2¹ protons are larger than the Zn 3¹-hydroxyalkyl chlorin and Zn 3¹-methoxyalkyl chlorin by Ganapathy

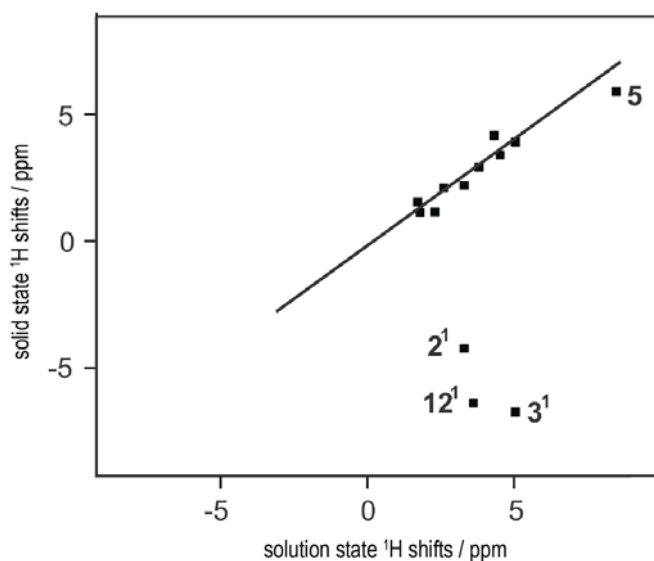


Figure 4.5. Chemical shift correlation plot of ZnChl. The ¹H shifts of the aggregates in Solid state NMR are plotted against the monomer shifts in THF-*d*₆. The solid line represents the diagonal. ¹H signals are indicated that show a large upfield shift in the solid relative to the monomer.

et al, and suggest that stronger lateral interactions occur²¹. This can be due to the formation of strong NH•••CO hydrogen bonds. The difference between the Zn 3¹-hydroxyalkyl chlorin and Zn 3¹-methoxyalkyl chlorin in terms of ring current shifts was quite small. Since only the hydroxy Zn chlorin can form OH•••CO hydrogen bonds, it was concluded that the hydrogen bonding for ZnChl had only a weak effect on the packing. Stronger hydrogen bonds with shorter bond lengths will increase the overlap of two neighboring rings, hence increase in the ring current effects.

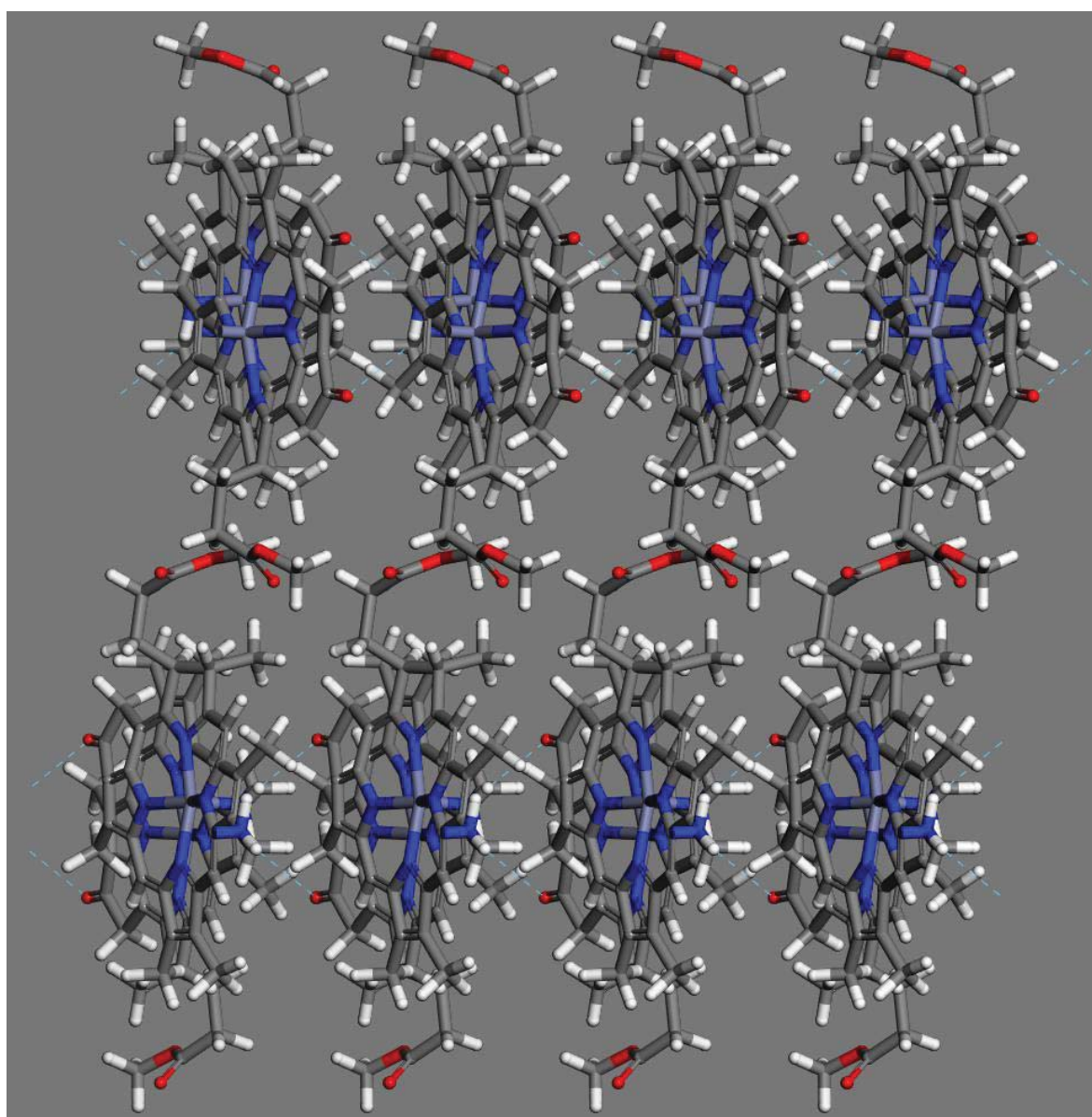


Figure 4.6. Geometry-optimized lateral associated *syn-anti* parallel stacks of 16 ZnChl molecules.

The molecule ZnChl is chiral, so it will accommodate in one of the chiral space groups. Among the chiral space groups, the most frequently encountered are P1, P2₁ and P2₁2₁2₁. Based on our previous explorations of natural chlorosomes, we conjecture that for a parallel stacking the P2₁ packing is likely, since it allows for stacks running parallel in planes, with the planes running in opposite directions to cancel the overall electric dipole in the 3D structure^{34,35}. The screw and monoclinic cell allows for shifting the planes relative to one another to optimize the packing of the 17¹ side chains to increase the density to 1.25 g/cm³ which would be difficult to achieve within an orthorhombic arrangement. This density is in the range for organic compounds and is close to the 1.31 g/cm³ determined for Ethyl Chlorophyllide *a* Dihydrate for which an X-ray structure is available³⁶.

In Pandit *et al.* it was noted that the NMR results could not discriminate between formation of vertically stacked a *syn-anti* dimers and anti-parallel stacks, because the orientation of the Zn chlorin molecules in the respective models was very similar, hence, produced the same ring current effects²². Alternatively to anti-parallel stacking, the ZnChl in this study may form stacked fibers of laterally associated *syn-anti* dimers, stabilized by hydrogen bonds.

The experimental ¹³C NMR chemical shifts for slabs of ZnChl stack and calculated chemical shifts using CASTEP code are showed in Table 4.3. The RMSD is 5.26, which is not unusual for moderately large molecules³⁷.

Chapter 4

Table 4.3. ^{13}C chemical shifts for ZnChI, experimental values in solid state ($\sigma_s^{\text{C}_{\text{expt}}}$), calculated chemical shifts with CASTEP code ($\sigma_s^{\text{C}_{\text{cal}}}$) and the deviation.

Position	$\sigma_s^{\text{C}_{\text{expt}}}$	$\sigma_s^{\text{C}_{\text{cal}}}$	Deviation
13 ¹	192.87	200.01	-7.14
17 ³	174.02	181.74	-7.72
19	165.49	168.30	-2.81
14	160.61	165.86	-5.25
16	154.09	160.73	-6.64
1	154.09	155.27	-1.18
6	151.23	154.03	-2.80
4	148.67	147.94	0.73
11	148.67	152.47	-3.80
9	145.32	150.75	-5.43
8	144.85	140.70	4.15
3	140.88	136.96	3.92
2	131.63	134.93	-3.30
7	131.63	138.03	-6.40
12	131.63	134.66	-3.03
13	131.63	132.35	-0.72
10	104.70	103.82	0.88
15	104.70	107.29	-2.59
5	93.91	96.72	-2.81
20	88.83	94.05	-5.22
3 ¹	29.05	30.79	-1.74
17	51.39	51.52	-0.13
18	48.46	50.88	-2.42
17 ⁴	51.39	50.84	0.55
13 ²	48.46	47.35	1.11
17 ²	30.41	31.70	-1.29
17 ¹	29.35	31.55	-2.20
18 ¹	23.36	16.80	6.56
8 ¹	18.54	6.41	12.13
8 ²	18.16	6.41	11.75
7 ¹	10.42	4.16	6.26
2 ¹	10.42	-1.81	12.23
12 ¹	3.78	2.77	1.01
13 ¹	192.87	200.01	-7.14

RMSD 5.26

4.4. Conclusion

The here presented data on a new type of ZnChl compound contribute to the experimental underpinning of the library of stack modes for self-aggregated semi synthetic Zn chlorins. We demonstrate that the small change of removing the 3³ methyl group of Zn 3¹-aminomethyl chlorin has a significant effect on the self-assembly of this compound. The resulting aggregates form laterally associated *syn-anti* parallel stacks with tight packing interactions, explained by the formation of strong hydrogen bonds and the small amino motif. Solid-State NMR analysis provides a direct link between subtle modifications in the chemical structure and alterations in the resulting packing structure. This approach, in which novel dye molecules can be rapidly screened for functionality in terms of their self-assembly interactions without the need for isotope label incorporation, will further advance the new generation of artificial leaf systems.

4.5. References

1. Martinez-Planells, A. *et al.* Determination of the topography and biometry of chlorosomes by atomic force microscopy. *Photosynth. Res.* **71**, 83–90 (2002).
2. Saga, Y., Shibata, Y., Itoh, S. & Tamiaki, H. Direct Counting of Submicrometer-Sized Photosynthetic Apparatus Dispersed in Medium at Cryogenic Temperature by Confocal Laser Fluorescence Microscopy: Estimation of the Number of Bacteriochlorophyll c in Single Light-Harvesting Antenna Complexes Chloros. *J. Phys. Chem. B* **111**, 12605–12609 (2007).
3. Montaña, G. A. *et al.* Characterization of *Chlorobium tepidum* chlorosomes: a calculation of bacteriochlorophyll c per chlorosome and oligomer modeling. *Biophys. J.* **85**, 2560–2565 (2003).
4. Psencík, J. *et al.* Lamellar organization of pigments in chlorosomes, the light harvesting complexes of green photosynthetic bacteria. *Biophys. J.* **87**, 1165–1172 (2004).
5. Sengupta, S. & Würthner, F. Chlorophyll J-Aggregates: From Bioinspired Dye Stacks to Nanotubes, Liquid Crystals, and Biosupramolecular Electronics. *Acc. Chem. Res.* **46**, 2498–2512 (2013).
6. Sridharan, A., Muthuswamy, J. & Pizziconi, V. B. Optoelectronic Energy Transfer at Novel Biohybrid Interfaces Using Light Harvesting Complexes from *Chloroflexus aurantiacus*. *Langmuir* **25**, 6508–6516 (2009).
7. Scholes, G. D., Fleming, G. R., Olaya-Castro, A. & van Grondelle, R. Lessons from nature about solar light harvesting. *Nat. Chem.* **3**, 763–774 (2011).
8. Eisenmayer, T. J., de Groot, H. J. M., van de Wetering, E., Neugebauer, J. & Buda, F. Mechanism and Reaction Coordinate of Directional Charge Separation in Bacterial Reaction Centers. *J. Phys. Chem. Lett.* **3**, 694–697 (2012).
9. Prokhorenko, V. I., Steensgaard, D. B. & Holzwarth, A. R. Exciton dynamics in the chlorosomal antennae of the green bacteria *Chloroflexus aurantiacus* and *Chlorobium tepidum*. *Biophys. J.* **79**, 2105–2120 (2000).

10. Nishimori, R., Mizoguchi, T., Tamiaki, H., Kashimura, S. & Saga, Y. Biosynthesis of Unnatural Bacteriochlorophyll c Derivatives Esterified with α,ω -Diols in the Green Sulfur Photosynthetic Bacterium *Chlorobaculum tepidum*. *Biochemistry* **50**, 7756–7764 (2011).
11. Saga, Y., Hirota, K., Harada, J. & Tamiaki, H. In Vitro Enzymatic Activities of Bacteriochlorophyll a Synthase Derived from the Green Sulfur Photosynthetic Bacterium *Chlorobaculum tepidum*. *Biochemistry* **54**, 4998–5005 (2015).
12. Saga, Y., Takahashi, N., Miyatake, T. & Tamiaki, H. Amphiphilic zinc bacteriochlorophyll a derivatives that function as artificial energy acceptors in photosynthetic antenna complexes chlorosomes of the green sulfur photosynthetic bacterium *Chlorobaculum limnaeum*. *J. Photochem. Photobiol. A Chem.* **353**, 612–617 (2018).
13. Mizoguchi, T., Kinoshita, Y., Harada, J. & Tamiaki, H. Supramolecular Organogelation of Bacteriochlorophyll-c Possessing an Isobutyl Substituent at the 8-Position in Carbon Tetrachloride. *Chempluschem* **82**, 595–597 (2017).
14. Sengupta, S. *et al.* Biosupramolecular Nanowires from Chlorophyll Dyes with Exceptional Charge-Transport Properties. *Angew. Chemie Int. Ed.* **51**, 6378–6382 (2012).
15. Patwardhan, S., Sengupta, S., Siebbeles, L. D. A., Würthner, F. & Grozema, F. C. Efficient Charge Transport in Semisynthetic Zinc Chlorin Dye Assemblies. *J. Am. Chem. Soc.* **134**, 16147–16150 (2012).
16. Harputlu, E., Ocakoglu, K., Yakuphanoglu, F., Tarnowska, A. & Gryko, D. T. Physical properties of self-assembled zinc chlorin nanowires for artificial light-harvesting materials. *Nano-Structures & Nano-Objects* **10**, 9–14 (2017).
17. Ilshadsabah, A. & Suchithra, T. V. Bacterial Nanowires: An Invigorating Tale for Future BT - Microbial Nanobionics: Volume 2, Basic Research and Applications. in (ed. Prasad, R.) 77–88 (Springer International Publishing, 2019). doi:10.1007/978-3-030-16534-5_5
18. Tamiaki, H. Supramolecular structure in extramembraneous antennae of green photosynthetic bacteria. *Coord. Chem. Rev.* **148**, 183–197 (1996).
19. Ganapathy, S. *et al.* Alternating syn-anti bacteriochlorophylls

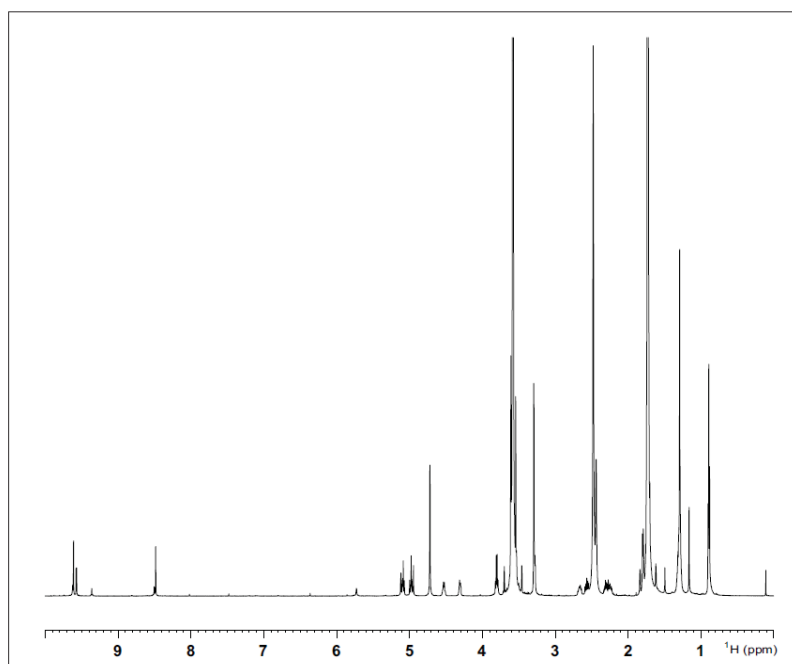
Chapter 4

- form concentric helical nanotubes in chlorosomes. *Proc. Natl. Acad. Sci.* **106**, 8525 LP – 8530 (2009).
20. Huber, V., Sengupta, S. & Würthner, F. Structure–Property Relationships for Self-Assembled Zinc Chlorin Light-Harvesting Dye Aggregates. *Chem. – A Eur. J.* **14**, 7791–7807 (2008).
 21. Ganapathy, S. *et al.* Zinc chlorins for artificial light-harvesting self-assemble into antiparallel stacks forming a microcrystalline solid-state material. *Proc. Natl. Acad. Sci.* **106**, 11472 LP – 11477 (2009).
 22. Pandit, A. *et al.* Structure Determination of a Bio-Inspired Self-Assembled Light-Harvesting Antenna by Solid-State NMR and Molecular Modeling. *J. Phys. Chem. B* **117**, 11292–11298 (2013).
 23. Harputlu, E., Ince, M. & Ocakoglu, K. Investigation of self-aggregation properties of amino functionalized zinc chlorins. *Appl. Surf. Sci.* **422**, 348–353 (2017).
 24. Tamiaki, H., Holzwarth, A. R. & Schaffner, K. Dimerization of synthetic zinc aminochlorins in non-polar organic solvents. *Photosynth. Res.* **41**, 245–251 (1994).
 25. Lee, M. & Goldberg, W. I. Nuclear-Magnetic-Resonance Line Narrowing by a Rotating rf Field. *Phys. Rev.* **140**, A1261–A1271 (1965).
 26. Pickard, C. J. & Mauri, F. All-electron magnetic response with pseudopotentials: NMR chemical shifts. *Phys. Rev. B* **63**, 245101 (2001).
 27. Yates, J. R., Pickard, C. J. & Mauri, F. Calculation of NMR chemical shifts for extended systems using ultrasoft pseudopotentials. *Phys. Rev. B* **76**, 24401 (2007).
 28. Profeta, M., Mauri, F. & Pickard, C. J. Accurate First Principles Prediction of 17O NMR Parameters in SiO₂: Assignment of the Zeolite Ferrierite Spectrum. *J. Am. Chem. Soc.* **125**, 541–548 (2003).
 29. Joyce, S. A., Yates, J. R., Pickard, C. J. & Mauri, F. A first principles theory of nuclear magnetic resonance J-coupling in solid-state systems. *J. Chem. Phys.* **127**, 204107 (2007).
 30. Dumez, J.-N. & Pickard, C. J. Calculation of NMR chemical shifts in organic solids: Accounting for motional effects. *J. Chem. Phys.* **130**, 104701 (2009).
 31. Zurek, E., Pickard, C. J. & Autschbach, J. Determining the Diameter of Functionalized Single-Walled Carbon Nanotubes with ¹³C NMR: A Theoretical Study. *J. Phys. Chem.*

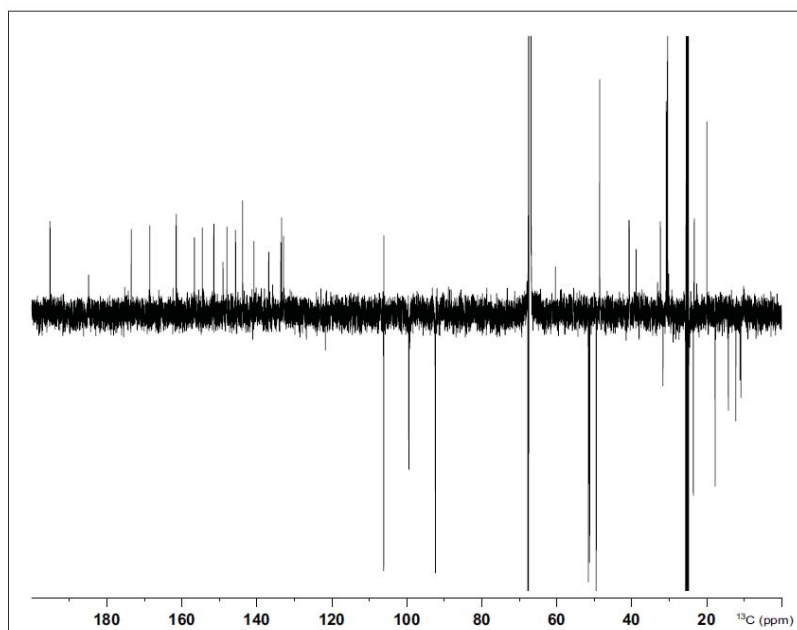
- C* **112**, 9267–9271 (2008).
32. Ido de Boer, Jörg Matysik, Kees Erkelens, Shin-ichi , Sasaki Tomohiro, Miyatake Shiki YagaiHitoshi Tamiaki, Alfred R. Holzwarth, H. J. M. de G. MAS NMR Structures of Aggregated Cadmium Chlorins Reveal Molecular Control of Self-Assembly of Chlorosomal Bacteriochlorophylls. *J. Phys. Chem. B* **108**, 16556–16566 (2004).
 33. Miyatake, T. & Tamiaki, H. Self-aggregates of natural chlorophylls and their synthetic analogues in aqueous media for making light-harvesting systems. *Coord. Chem. Rev.* **254**, 2593–2602 (2010).
 34. Thomas, B. *et al.* Determination of Controlled Self-Assembly of a Paracrystalline Material by Homology Modelling with Hybrid NMR and TEM. *Chem. – A Eur. J.* **23**, 9346–9351 (2017).
 35. de Boer, I. *et al.* MAS NMR Structure of a Microcrystalline Cd-Bacteriochlorophyll d Analogue. *J. Am. Chem. Soc.* **125**, 13374–13375 (2003).
 36. Chow, H.-C., Serlin, R. & Strouse, C. E. Crystal and molecular structure and absolute configuration of ethyl chlorophyllide a-dihydrate. Model for the different spectral forms of chlorophyll a. *J. Am. Chem. Soc.* **97**, 7230–7237 (1975).
 37. Hofstetter, A. & Emsley, L. Positional Variance in NMR Crystallography. *J. Am. Chem. Soc.* **139**, 2573–2576 (2017).

4.6. Appendix

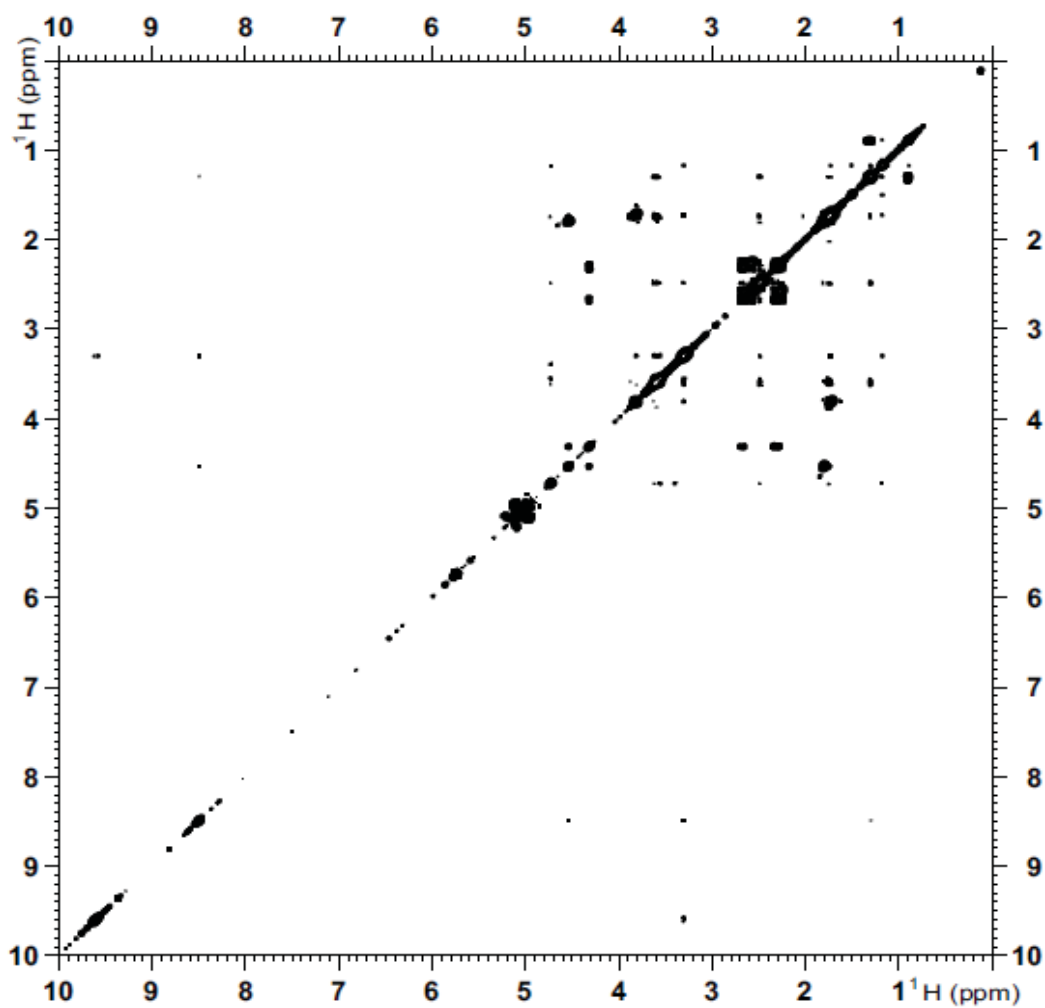
Figure 4A.1 ^1H NMR spectra of ZnChl in THF- d_8



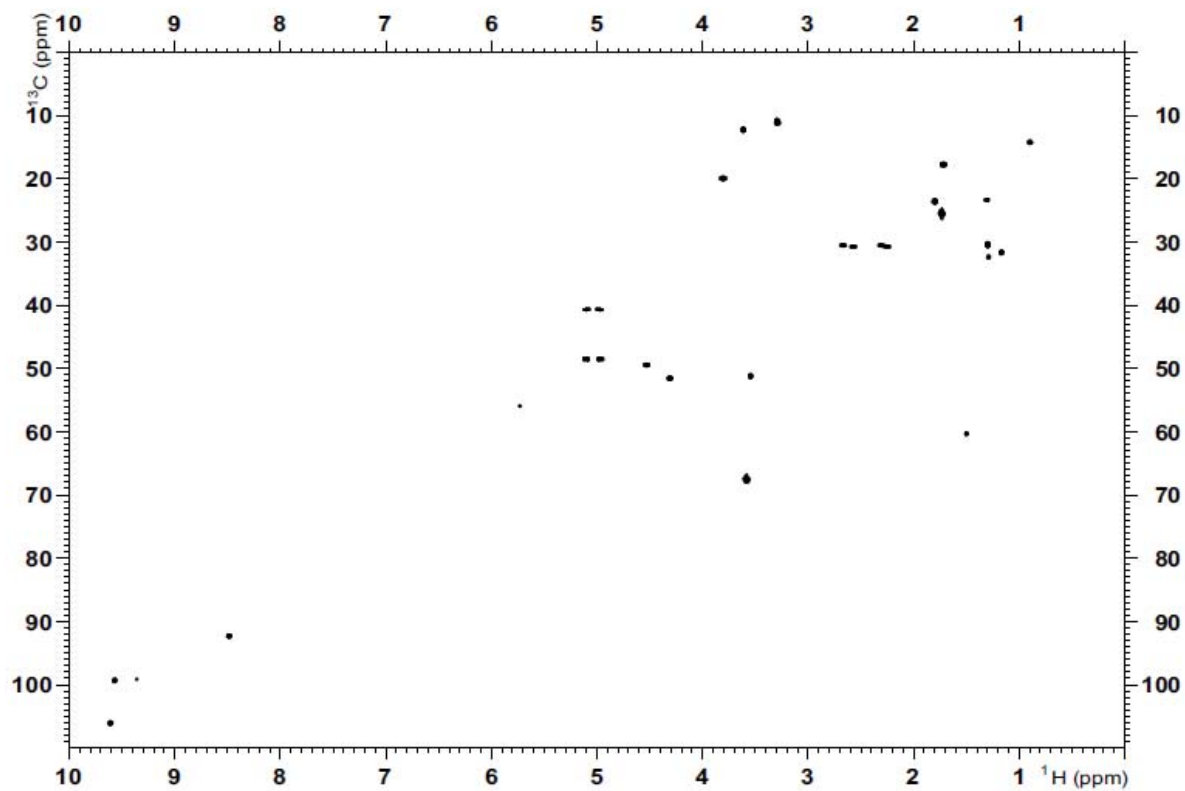
Appendix 4A.2. ^{13}C APT NMR spectra of ZnChl aminochlorin in THF- d_8



Appendix 4A.3. ¹³C-¹H COSY spectrum of ZnChl aminochlorin in THF-*d*₈



Appendix 4A.4. ^{13}C - ^1H HSQC spectrum of ZnChl aminochlorin in $\text{THF-}d_8$



Conclusions and Outlook

The human race, since civilizations started, made many technological, scientific and economic advancements. However, at present mankind is running up against a wall, because of reaching global limitations with respect to food, energy, and natural resources. The population on earth is going to increase, and together with raising standards of living this makes that the demand for resources and energy also increases. Nevertheless, scientists believe that nature can provide us with solutions. Much about how to include sustainability in an efficient energy system can be learned from natural photosynthesis. Nature evolved the tetramanganese cluster in photosynthesis to oxidize water and store energy in the form of chemical compounds made from atmospheric CO₂. This central motif did not change despite the diversities in soil, environments and climatic conditions across earth. In principle, sustainability in energy can be provided in the form of artificial photosynthesis (AP). To design AP systems, however, it is necessary to understand first how natural photosynthesis works at the molecular level, so that we can mimic and create artificial leaves. This thesis is about elements that can contribute to gaining fundamental understanding, by analyzing water oxidation in time with a new experimental setup, by resolving how cells modulate collection of photons in a light harvesting antenna, and by transferring principles of natural light collection to semi-artificial light harvesting systems. While rebuilding the energy system may turn out to be the grandest challenge mankind is currently facing, it is to be realized by new inventions and progress made by individual scientists, step by step.

Regarding water oxidation, finding the transient intermediate in the S₃⁺ to S₀ⁿ step of the water oxidation mechanism of Photosystem II is a Holy Grail in Photosynthetic research. A crucial hurdle is to develop methodology to study the molecular mechanism of water oxidation reaction in time. Chapter 2 describes the design and construction of a three-flash flow cell enable the study of single or multiple flash activated photochemical reactions. The novel methodology of flash flow RFQ-EPR is implemented on Photosystem II particles made from spinach. The current setup can produce three sequential flashes of 10 μs each by using lights source of 680 nm diode lasers, which drive Photosystem II through the Kok cycle. The dead time is 2.0 ± 0.3 ms using liquid isopentane, maintaining at a temperature of 140K as cryomedium. The intermediate states

Chapter 5

during water oxidation reaction of Photosystem II, S_2^+ , S_3^+ and S_0^n are characterized by EPR spectroscopy. For faster freezing, the nozzle diameter can be reduced and doing experiments in vacuum can remove oxygen signal from EPR spectrum, these are for future experiments.

The role of arginine-glutamate (Arg-Glu) ion pairs are explored in the switch between the light harvesting and photoprotection modes of Major light harvesting complexes. In chapter 3 a non-invasive method to analyze the Arg structures of the major light-harvesting complex II (LHCII) by using Magic-Angle Spinning (MAS) NMR and selective Arg isotope enrichment in cc-424 mutant of *Chlamydomonas reinhardtii*. The conformations of the Arg residues that interlock helix A and B appear to be preserved in the light-harvesting and photoprotective state.

In Chapter 4 the molecular packing of an artificial light-harvesting antenna self-assembled from 3¹-aminofunctionalized zinc-chlorins was determined by MAS NMR. Ring-current NMR chemical shifts provided spatial constraints and together with quantum-mechanical modeling this allowed us to build a molecular-stack model in silico. Anomalously large ¹H aggregation shifts up to 11.4 ppm were observed, which reveal a closely packed stacking of molecules in the aggregate structure. The method does not require isotope enrichment or crystallization and is generally applicable to determine de novo self-assembled structures of aromatic molecules with structural asymmetry, such as is commonly provided by functionalized side chains that serve to tune the self-assembly process. Electron diffraction studies which can reveal the 3D structure of these studied Zn chlorines can be the future experiments.

In the coming years, it can be anticipated that these steps will be made, when many more researchers focus on fulfilling the fundamental research needs of artificial photosynthesis.

Appendices

Summary

Decentralized plug and play systems for energy production are the future picture of our society. Artificial photosynthetic systems are used for this purpose. These systems are inspired by natural photosynthesis. Natural photosynthesis contains tetramanganese clusters to oxidize water and store the energy in the form of chemical compounds from atmospheric CO₂.

Chapter 2 illustrates the detailed construction of a three-flash flow cell to study light induced biological reactions, specifically the water oxidation reaction of Photosystem II. This instrument is capable of producing the S₂⁺, S₃⁺ and S₀ⁿ intermediate states of the Kok cycle. I confirmed these by EPR experiments. The dead time is 2 ms for this instrument, which is the time between the last flash and hyperquenching of the sample by freezing using liquid isopentane as cryomedium.

In chapter 3, I study the mechanism of the major LHC II involved in conformational switching from light harvesting to the photoprotective state, in which excess light is dissipated as heat. I use MAS NMR as a non-invasive method to understand the structure and environment around Arg residues in *Chlamydomonas reinhardtii* LHC II. In this approach the Arg amino acid is selectively labeled with ¹³C isotopes. Solid state NMR results shows that the conformations of the Arg residues are preserved in both the light harvesting and the photoprotective state. These residues are found in the α-helical regions near the stromal site and in the interlocked core of LHC II complex.

Chapter 4 studies the structure of self-aggregated semi synthetic Zn 3¹ amino chlorin that forms syn-anti parallel stacks according to the solid state NMR data. The small change of removing 3³ methyl group of Zn 3¹ aminomethyl chlorin has significant effect on self-assembly. Solid State NMR analysis provides a direct link between subtle modification in the chemical structure and alterations in resulting packing structure.

Finally, chapter 5 provides an outlook on what steps can be performed next in hyperfreeze quenching NMR, LHCII studies, and artificial aggregates, based on the work presented in this thesis.

Samenvatting

Gedecentraliseerde plug-and-play-systemen voor energieproductie zijn het toekomstbeeld van onze samenleving. Hiervoor worden kunstmatige fotosynthesesystemen gebruikt. Deze systemen zijn geïnspireerd op natuurlijke fotosynthese. Natuurlijke fotosynthese bevatten tetramangaan clusters om water te oxideren en de energie op te slaan in de vorm van chemische verbindingen uit atmosferisch CO₂.

Hoofdstuk 2 beschrijft de gedetailleerde constructie van een door drie-licht flitsen geactiveerde stroomcel om door licht geïnduceerde biologische reacties te bestuderen, in het bijzonder de wateroxidatiereactie van fotosysteem II. Dit instrument kan de S₂⁺, S₃⁺ en S₀ⁿ tussenliggende toestanden van de Kok-cyclus produceren. Ik bevestigde deze door EPR-experimenten. De dode tijd is 2 ms voor dit instrument, wat de tijd is tussen de laatste flits en hyperquenching van het monster door bevriezing met vloeibaar isopentaan als cryomedium.

In hoofdstuk 3 bestudeer ik het mechanisme van de belangrijkste LHC II die betrokken is bij conformationele omschakeling van het oogsten van licht naar de fotoprotectieve toestand, waarin overtollig licht wordt gedissipeerd als warmte. Ik gebruik MAS NMR als een niet-invasieve methode om de structuur en omgeving rond Arg-residuen in *Chlamydomonas reinhardtii* LHC II te begrijpen. In deze benadering wordt het Arg-aminozuur selectief gemerkt met ¹³C-isotopen. Vaste stof NMR toont aan dat de conformaties van de Arg-residuen behouden blijven in zowel de lichttoogst als de fotoprotectieve staat. Deze residuen bevinden zich in de alpha-helix gebieden nabij de stomale plaats en in de met elkaar verbonden helices in de kernen van het LHC II complex.

Hoofdstuk 4 bestudeert de structuur van zelf-geaggregeerde semi-synthetische Zn ³¹-aminochlorines die syn-anti parallelle stapels vormen volgens de vaste toestand NMR metingen. De kleine verandering van het verwijderen van de ³³-methylgroep van Zn ³¹-aminomethylchlor heeft een aanzienlijk effect op de zelfassemblage. Vaste stof NMR-

analyse laat een direct verband zien tussen de subtiele modificatie van de chemische structuur en wijzigingen in de resulterende pakking.

Hoofdstuk 5 ten slotte geeft een overzicht van de stappen die in de toekomst kunnen worden gezet met hyperfreeze quenching, LHCII-onderzoek en vaste stof NMR aan kunstmatige aggregaten, gebaseerd op het werk gepresenteerd in dit proefschrift.



Curriculum Vitae

I was born in Dharmavaram, Andhra Pradesh, India on July 20, 1986. After, I finished my schooling, I obtained my bachelor's degree in Chemistry from Sri Krishna Devaraya University, Anantapur, India. After completion of bachelor's degree in 2006, I started my Master Degree program in July 2007 at Indian Institute of Technology Madras. I completed my Masters degree with dissertation titled as "Implementation of 2D LASSY for ^{183}W NMR" under the supervision of Prof. Dr. N. Chandra Kumar. In September 2009, I started my doctoral studies in the Biophysical Organic Chemistry group at Leiden University under the supervision of Prof. dr. H. J. M. de Groot. My research work was presented as posters at various national and international conferences like Euromar, Ireland 2012, NMR discussion group, DSM Delft, 2011, BioSolar Cells annual meeting 2012 and 2013. I received best oral presentation award at Eurocores meeting, Bologna, Italy in 2012.

Acknowledgments

The time has arrived for me to thank so many people, who supported me emotionally, intellectually, financially, morally or hypothetically during or after my PhD career. The ever-inspiring idea of pursuing a career in science came to my mind when I first visited well-established research labs at Indian Institute of Science Bengaluru (IISc), India. I have fulfilled it by joining as a promovendus in Leiden University. First of all, my sincere gratitude goes to Prof. Huub for giving me an opportunity to express my scientific dream, for which I shall be indebted forever. You gave me a freedom to express my opinions and patiently listening to them during our regular scientific discussions. You recognized my talent as a good presenter and encouraged me to further strengthen my skills in giving a better scientific talk. Due to all of your efforts, I am now proudly can say that I am working as a “Teacher” in a college (which is equivalent to hbo in Netherlands) back at home in India. As a part of PhD life, I have had ups and downs like many others yet I enjoyed it with a great pleasure. The beautiful memories and incidents that I have encountered as a PhD student are now helping me to train the future generation in India.

I extend my sincere thanks to late Simon, who taught me how to be a dedicated scientist. Your unparalleled enthusiasm in the laboratory encouraged me to perform all experiments with a great passion. Your never lose hope attitude helped me to overcome my work-related stress and motivated me to perform better at work even though when experiments were not going as planned. Unfortunately, we scientific community lost a gem like you.

I would like to thank my co-promoter Anjali for her tremendous support from Vrije Universiteit Amsterdam. We had so many interesting and fruitful scientific discussions on LHCII, which led to a very nice publication in Journal of Biological Chemistry. I have enjoyed working with you and due to your continuous motivation, I have now a thesis in good shape.

I thank all SSNMR/BPOC group members for their support during my stay in Leiden. Liesbeth, I still remember my first day in Netherlands when you came to receive me from Schiphol. I appreciate your help in visa related work. I can proudly say that you are the heart of our group. Karthick anna, thank you very much for your help both in and out of the lab. I have learned cooking a delicious food from you. Brijith, I never forgot our discussions on not only on science but also on very interesting like agriculture, economy

during our lunch and coffee breaks. I also thank my colleagues at work Smitha, Firat, Adriano, Thomas, Vidya, Fons, Yohan, Yuliya, Alia, Franco, Dario, Jan Paul, Tirong, Zhongwu, Rubin, Maithili, Faezeh, Dipen, Remco, Xinmeng, Yang Shao thank you all for your support. I further extend my thanks to Sateesh from Wageningen for wonderful trips within and outside of Netherlands. Thanks Laura for Dutch translation of summary.

To be ever successful either in professional or personal life, it is only possible if you have a full support from family. I am happy to count myself as one of those lucky people who as a great support from parents and brothers. Last but not least I want to thank the special person in my life i.e. my lovable wife Prabhallika for standing beside me in both happy and hard times during my PhD. Furthermore, you gave me two sweetest gifts for life in the form of our children Satvik and Geetanshi. They are the reason for us to smile every second in our life.

Publications

1. “Insights in the photoprotective switch of the major Light-Harvesting Complex II (LHCII): A preserved core of arginine-glutamate interlocked helices complemented by adjustable loops.” Kiran Sunku, Huub. J. M. de Groot, Anjali Pandit, *The Journal of Biological Chemistry*, 2013, 288, 19796-19804.
2. “Design of a novel device enabling freeze-quench trapping of laser flash activated Photosystem II intermediates.” Kiran Sunku, Hans J. van Gorkom, Simon de Vries, Huub. J. M. de Groot. (Manuscript in preparation)
3. “Structure determination of self-aggregated and semi synthetically prepared Zn ³-amino chlorin with MAS NMR and molecular modelling.” Kiran Sunku, Naoto Kuwamura, Brijith Thomas, Alfred R. Holzwarth, Anjali Pandit, Huub. J. M. de Groot. (Manuscript in preparation)
4. “Characterization of Polymer-Ceramic Nanocomposites for Advanced Applications.” Kiran Sunku, Satesh Gangarapu, Mohd Rafie Johan, Putla Sudarsanam. *Handbook of Polymer and Ceramic Nanotechnology*, Springer, 2019,1-16.
5. “Fabrication of polymer-graphene nanocomposites.” Kiran Sunku, Satesh Gangarapu, Mohd Rafie Johan, Putla Sudarsanam. *Handbook of Polymer and Ceramic Nanotechnology* (Book chapter accepted) Springer, 2019.